AFRL-SR-AR-TR-04-

0624

REPORT DOCUMENTATION PAGE

1. REPORT DATE (DD-MM-YYYY) 01/12/2004	2. REPORT TYPE Final Technical	3. DATES COVERED (From - To) April 2001 – September 2004

4. TITLE AND SUBTITLE	5a. CONTRACT NUMBER
Shear Layer Dynamics in Resonating Cavity Flows	F496620-01-1-0326
	5b. GRANT NUMBER
	5c. PROGRAM ELEMENT NUMBER

6. AUTHOR(S)	5d. PROJECT NUMBER
Lawrence Ukeiley and Nathan Murray	
	5e. TASK NUMBER
	5f. WORK UNIT NUMBER

7. PERFORMING ORGANIZATION NAME(S) AND ADDRESS(ES)	8. PERFORMING ORGANIZATION REPORT NUMBER
University of Mississippi Jamie Whitten National Center for Physical Acoustics University, Mississippi, 38677	

9. SPONSORING / MONITORING AGENCY NAME(S) AND ADDRESS(ES)	10. SPONSOR/MONITOR'S ACRONYM(S)
Dr. John Schmisseur AFOSR/NA	AFOSR
4015 Wilson Boulevard Room 713 Arlington, VA 22203-1954	11. SPONSOR/MONITOR'S REPORT NUMBER(S) F496620-01-1-0326

12. DISTRIBUTION / AVAILABILITY STATEMENT
Approved for public release; distribution unlimited.

13. SUPPLEMENTARY NOTES

14. ABSTRACT
The shear layer above open cavities were studied through detailed velocity and surface pressure measurements sampled in a synchronous manner. The Particle Image Velocimetry measurement yielded mean flow characteristics and instantaneous flow snapshots. The mean turbulent quantities showed the dominance of the shear layer and the region around the corner of the aft wall. Cross-correlations of the surface pressure measurements showed evidence of the shear layer structures being convected downstream and an upstream propagating acoustic wave for the cases where resonance occurred. The PIV data was also combined with the surface pressure measurements through the application of the Quadratic Stochastic Estimation procedure to provide time resolved snapshots of the flow field. Examination of these results indicate the strong pumping action of the cavity regardless of whether resonance existed and was used to visualize the large scale structures interacting with the aft wall.

15. SUBJECT TERMS
Cavity Flows, Stochastic Estimation

16. SECURITY CLASSIFICATION OF:			17. LIMITATION OF ABSTRACT	18. NUMBER OF PAGES	19a. NAME OF RESPONSIBLE PERSON
a. REPORT UNCLASSIFIED	b. ABSTRACT UNCLASSIFIED	c. THIS PAGE UNCLASSIFIED	UU		19b. TELEPHONE NUMBER (include area code)

Standard Form 298 (Rev. 8-98)
Prescribed by ANSI Std. Z39.18

Final Technical Report

Shear Layer Dynamics in Resonating Cavity Flows

Lawrence Ukeiley and Nathan Murray

Jamie Whitten National Center for Physical Acoustics
University of Mississippi

1 Introduction

Fluid flow over cavities has been a topic of research since the 1950's. The complexity and broad range of cavity flows offers a great challenge in trying to gain a full understanding of the flow physics. The present work is driven by a desire to control and reduce the broadband pressure loads inside the cavity. However, before such a monumental task can be efficiently accomplished it is important to develop a better understanding of the relevant dynamical events.

A review of the literature reveals important general characteristics of cavity flows. In one of the earliest works on cavity flows, Roshko (1955) makes two notable conclusions. First, the increase in drag caused by the cavity is due totally to the pressures on the cavity walls. Therefore, in order to balance any unsteady pressures there must be a net momentum flux into and out of the cavity. This momentum flux is often described as a "breathing" or "pumping" action. Second, the fluctuation of the stagnation streamline causes a variation in the pressure at the back wall. This fluctuation in pressure creates a source for sound production at the aft cavity wall. Rossiter's (1964) landmark work on cavity flow yielded an empirical formula that allows the possible resonant mode frequencies to be predicted:

$$ f = \frac{U}{L} \frac{(m - \gamma)}{(\frac{1}{\kappa} + Ma)} \qquad m = 1,2,3,\dots \qquad \text{1-1} $$

Here f is frequency, U is the free stream velocity, L is the cavity length, Ma is the Mach number, κ is the ratio of the convection velocity of structures in the shear layer to the free stream velocity, m is the mode number, γ is an empirical constant set to 0.25. Rossiter found κ to be 0.57 independent of cavity configuration.

Many other important works have been published by Heller, Holmes, and Covert (1971); Block (1976); Tam and Block (1978) ; Hardin and Mason (1977); Krishnamurty (1955); Heller and Bliss (1975); Bilanin and Covert (1973); Tracy and Plentovich (1997); Disimile, Toy and Savory (2000).

For a general review of cavity flow mechanics see the review of Rockwell and Naudascher (1978) or Murray (2003). For a review of cavity flow control see Cattafesta, Williams, Rowley, and Alvi (2003). A review of these works leads to several important observations concerning the aeroacoustics of cavity flows:

- Cavity flow aeroacoustics is determined by the coupling of the shear-layer instabilities with the acoustic properties of the cavity.
- Interaction of the shear-layer with the aft cavity wall causes a pressure fluctuation on this cavity boundary. This pressure fluctuation causes the downstream wall to act as an acoustic source.
- A feedback loop is created between the shear-layer and the downstream wall pressure source via the interaction of the radiated acoustic waves with the shear-layer. While shear-layer instabilities and wall pressure fluctuations

exist for all flow conditions, their existence does not guarantee a resonant condition.

- Existence of a resonant condition is governed by several quantities: (1) length to depth ratio (l/d), (2) cavity volume, (3) ratio of boundary layer thickness to cavity depth (δ/D), (4) Mach number of the free-stream flow, (5) Reynold's Number,(6) ratio of shear-layer convection velocity to free-stream velocity (κ), (7) temperature ratio between the cavity and the free-stream, and (8) the state of the incoming boundary layer as either laminar or turbulent.
- The cavity wall pressure and the radiated noise include both broadband and tonal components.

The above observations demonstrate the complexity of the flow and the resulting difficulty that lies in attempting to control the flow. The present study is part of a larger effort to produce a low-dimensional model for use in actively controlling this complex flow.

In working toward an active control scheme, cavity flows need to be examined based on measurements that can be made in real time. For example, it might be possible to identify a flow regime by examining the full-field velocity results from a PIV experiment, but such a measurement is not possible for real time flow control. Therefore, evaluation of measurements such as the wall pressure is key to later developing a low-dimensional model because of the ability to make and include such measurements in a real-time control scheme. Furthermore, the current study along with the recent work of Bassioni et al. (2004) suggests that the cavity flow mode can be identified by examining the wall-pressure measurements. This places even higher importance on the study of these surface type measurements and their relationship to the surrounding flow.

In this manuscript PIV measurements of subsonic flow over two cavity configurations are studied along with the fluctuating surface pressure inside the cavity. First, the experimental facilities and methodologies will be discussed. Then, details of the velocity field and the statistical properties will be discussed for both of the cavity configurations. Next, details of velocity-to-pressure and pressure-to-pressure correlations will be presented. This is followed by discussion of an application of surface pressure based Quadratic Stochastic Estimation (QSE) and details of the time dependent estimated velocity fields examined. Finally, we summarize all the results and draw some conclusions about the wall-pressure and velocity field.

2 Large-Scale Structure Techniques

Many of the techniques born out of the study of large-scale coherent structures have begun to be utilized for studying the dynamics of physical flow phenomena. Several examples of developing dynamical descriptions of flows based on low-dimensional descriptions were discussed in Glauser et al. (2000). The techniques discussed in that paper, like the ideas utilized in this work, are based on developing dynamical descriptions of flows utilizing minimal time-resolved information and significant statistical information. The work of Ukeiley et al. (1993) showed how POD and LSE could be used in a complementary fashion to develop a low-dimensional description of the structures in an axisymmetric jet. The works of Cole and Glauser (1998) and others have shown how LSE and POD alone and in the complementary

technique can be used to study time-dependent phenomena from limited time-dependent information and significant statistical information. These studies analyzed flows encountering sudden expansions, both planar and axisymmetric, and showed the time evolution of recirculation zones and the shear layer above them. More recently the work of Taylor (2001), Schmidt (2002) and Murray (2003) have shown the effectiveness of using surface measurements, pressure and shear stress respectively, as the quantity to estimate flow properties through what is termed the "modified complementary technique."

The current work has concentrated on an application of the Stochastic Estimation (Adrian, 1977) which is discussed in the next section. In addition we have performed an initial study to evaluate differences between stochastic estimation and the modified estimation procedure which is detailed in section 2.2.

2.1 Stochastic Estimation

As shown by Taylor (2001), Naguib, et al. (2001), and Picard & Delville (1999), a condition average of the velocity, $u_{ijx}(t)$, can be formulated using the time dependent wall pressure event, P(t), as the condition to yield an estimated velocity, $\tilde{u}_{ijx}(t)$:

$$\tilde{u}_{ijx}(t) = \left\langle u_{ijx}(t) \middle| P(t) \right\rangle \qquad \text{2-1}$$

The subscripts are used to denote the position, i and j (2-D flow), and the component, x, of the velocity that is of interest. Angle brackets denote ensemble averaging, and the velocities and pressures represent only the fluctuating components.

The conditional average can be estimated by a power series as shown by Guezennec (1989):

$$\tilde{u}_{ijx}(t) = A_{ijxk}P_k(t) + B_{ijxlm}P_l(t)P_m(t) + C_{ijxpqr}P_p(t)P_q(t)P_r(t) + \cdots \qquad \text{2-2}$$

The summation convention has been utilized, and the sum is taken from 1 to K where K is the number of estimating events (surface pressure measurements in this case).

2.1.1 Linear Stochastic Estimation

Retaining only the first term in equation 2-2, the linear estimate involves only one set of coefficients:

$$\tilde{u}_{ijx}(t) = A_{ijxk}P_k(t) \qquad \text{2-3}$$

The mean square error is defined in terms of the actual velocity:

$$e_{ijx}\left\langle \left(\tilde{u}_{ijx}(t) - u_{ijx}(t)\right)^2 \right\rangle \qquad \text{2-4}$$

The coefficients are found through a minimization of the mean square error by taking the derivative of (2-4) with respect to the coefficients and setting the result equal to zero:

$$\frac{\partial e_{ijx}}{\partial A_{ijxk}} \frac{\partial}{\partial A_{ijxk}} \left\langle \left(A_{ijxl} P_l(t+\tau) - u_{ijx}(t) \right)^2 \right\rangle = 0 \qquad k, l = 1, \cdots, K \qquad \text{2-5}$$

A time difference, τ, is introduced here for situations were the pressure and velocities are not measured at the same instant in time. This was necessary for application of the estimation to the experimental data presented later. The sensitivity of the pressure transducers to the PIV laser required that the pressure measurements be made slightly before the velocity measurements. For application to the simulation data discussed later, τ is set to zero. Carrying out the summation, equation 2-5 results in a set of K equations:

$$\left\langle 2\left(A_{ijxl} P_l(t+\tau) - u_{ijx}(t) \right) P_1(t+\tau) \right\rangle = 0$$
$$\vdots \qquad\qquad \text{2-6}$$
$$\left\langle 2\left(A_{ijxl} P_l(t+\tau) - u_{ijx}(t) \right) P_K(t+\tau) \right\rangle = 0$$

Carrying out the multiplication and rearranging yields the matrix equation for the coefficients:

$$\begin{bmatrix} A_{ijx1} \\ \vdots \\ A_{ijxK} \end{bmatrix} = \begin{bmatrix} \langle P_1(t+\tau)P_1(t+\tau) \rangle & \cdots & \langle P_K(t+\tau)P_1(t+\tau) \rangle \\ \vdots & \ddots & \vdots \\ \langle P_1(t+\tau)P_K(t+\tau) \rangle & \cdots & \langle P_K(t+\tau)P_k(t+\tau) \rangle \end{bmatrix}^{-1} \begin{bmatrix} \langle u_{ijx}(t)P_1(t+\tau) \rangle \\ \vdots \\ \langle u_{ijx}(t)P_K(t+\tau) \rangle \end{bmatrix} \qquad \text{2-7}$$

Equation 2-7 shows a set of K coefficients for every i, j, and x chosen. The first term on the right hand side is the inverse of a square matrix of two point pressure correlations. The second term on the right includes the correlations between the fluctuating velocity at a given ijx and the fluctuating wall pressure. Even though all the pressure measurement locations are included in the correlations, each individual correlation includes only a single pressure measurement.

The coefficients in Equation 2-7 are based solely on ensemble averaged correlations. Once these correlations are known and the coefficients are calculated, a set of pressure measurements and the coefficients can be applied in equation 2-3 to yield estimated velocities with the same time resolution as the input pressure measurement.

2.1.2 Quadratic Stochastic Estimation (QSE)

The quadratic estimate involves the first two terms of equation 2-2:

$$\tilde{u}_{ijx}(t) = A'_{ijxk} P_k(t+\tau) + B_{ijxlm} P_l(t) P_m(t+\tau) \qquad \text{2-8}$$

Due to the calculation of the coefficients, the linear and quadratic coefficients are not independent, so the coefficients for the linear term are different than the coefficients found in equation 2-7. A prime is used to distinguish between the two linear term coefficients. Following the procedure used to solve for the coefficients in the LSE, there

are two derivatives that need to be evaluated for the QSE because there are two sets of coefficients:

$$\frac{\partial e_{ijx}}{\partial A'_{ijxn}} = \frac{\partial}{\partial A'_{ijxn}}\left\langle\left(A'_{ijxk}P_k(t+\tau)+B_{ijxlm}P_l(t+\tau)P_m(t+\tau)-u_{ijx}(t)\right)^2\right\rangle = 0$$

$$\frac{\partial e_{ijx}}{\partial B_{ijxpq}} = \frac{\partial}{\partial B_{ijxpq}}\left\langle\left(A'_{ijxk}P_k(t+\tau)+B_{ijxlm}P_l(t+\tau)P_m(t+\tau)-u_{ijx}(t)\right)^2\right\rangle = 0$$

2-9

Carrying out the differentiation results in a set of equations that include both coefficients. Then if τ is required to be constant such that all the pressure measurements are collected at the same instant in time, some of these equations become linearly dependent because the interchange of subscripts doesn't have an effect on the result. A set of equations can be created to solve for the coefficients in terms of the 2_{nd} and 3_{rd} order correlations between velocity and pressure.

As with the LSE, this set of equations can be rearranged into a matrix equation to solve for the coefficients. The coefficient vector will be called $[AB]$. The pressure correlation matrix will be called $[PP]$, and the velocity/pressure correlation vector will be called $[VP]$:

$$[AB]_{ijx} = [PP]^{-1}[VP]_{ijx}$$

2-10

Each vector is of size Q and the matrix is a square symmetric matrix of size Q by Q where Q results from the possible number of combinations of subscripts:

$$Q = K + \sum_{i=0}^{K-1} K - i$$

2-11

As with LSE, there is a vector $[AB]$ and $[VP]$ for every ijx. Although this results in a large number of coefficients when applied to an entire 2-dimensional flow, the computational complexity is still much less than a time-dependent Navier-Stokes simulation. In contrast to LSE, the pressure correlation matrix $[PP]$ for QSE includes 2nd, 3rd and 4th order correlations between the pressure measurements while only 2nd order correlations were included in the LSE. $[VP]$ includes all of the correlations that were originally in the LSE. For the QSE, $[VP]$ also includes correlations between the velocity at ijx and two pressure measurement locations.

2.2 Modified Stochastic Estimation

In addition to using a surface pressure based stochastic estimation procedure we also investigated the use of a modified stochastic estimation. The modification comes from estimating the expansion coefficients from the Proper Orthogonal Decomposition (POD) then using them to reconstruct the velocity field. What follows is a brief introduction to the POD to help understand where these expansion coefficients come from.

Lumley (1967) introduced thr POD to the Fluid Dynamics community as a mathematically unbiased technique for determining coherent or large scale structures of turbulent flows. In its original formulation, the POD modes are the solution of a Fredholm integral eigenvalue problem that is derived from projecting a candidate set of modes onto an instantaneous field and may be written as follows:

$$\int_{\Omega} R_{ij}(\hat{x},\hat{x}')\phi_j^n(\hat{x}')d\hat{x}' = \lambda^n \phi_i^n(\hat{x}) \qquad \text{2-12}$$

The kernel of this equation, R_{ij}, is the two-point correlation tensor. The solution of the Fredholm equation yields a set of spatial eigenmodes that can be used to represent an unsteady flow field. The eigenfunctions can either be determined from solving the above equation or using the snapshot method (Sirovich, 1987), which greatly reduces the size of the eigenvalue problem for highly spatially resolved data sets. Hilbert-Schmidt (see Holmes et al, 1996) theory specifies that there is a denumerable set of the eigenmodes that are orthonormal and that the instantaneous field can be represented as an expansion coefficient multiplied by the spatial basis functions

$$u_i^n(\hat{x},t) = \sum_n a^n(t)\phi^n(\hat{x}) \qquad \text{2-13}$$

where the expansion coefficient is calculated from

$$a^n(t) = \int_{\Omega} u_i(\hat{x},t)\phi_i^n(\hat{x})d\hat{x} \qquad \text{2-14}$$

This approach requires that the time-resolved instantaneous field is known at all spatial locations simultaneously. This condition is not always met, and one must use alternative methods, such as the stochastic estimation procedure discussed above, to determine the time dependence of the expansion coefficients.

In the modified estimation procedure these POD expansion coefficients are estimated in the same way that the velocity field is in the conventional stochastic estimation and can be written as;

$$\tilde{a}^n(t) = \langle a^n(t)|P(t)\rangle \qquad \text{2-15}$$

In a similar manner to what was detailed for the surface pressure based QSE the estimated POD expansion coefficient can be written as;

$$\tilde{a}^n(t) = A'_{ijxk}P_k(t+\tau) + B_{ijxlm}P_l(t)P_m(t+\tau) \qquad \text{2-16}$$

Where the estimation coefficients are now found from correlations between the POD expansion coefficients and the surface pressure instead of correlations between the velocity field and the pressure. Finally, equation 2-13 can be used with the estimated coefficients to obtain an estimated velocity field.

Although the techniques are similar in their approach there are several large differences in the actual applications. The main difference is that the modified stochastic estimation correlates the surface pressure with an integral property, the POD expansion coefficients, while the QSE correlates a local property (e.g., the velocity) at a given spatial location. Hence application of the MQSE requires full-field measurements that are readily available from the PIV measurements such as those that will be described later in this document. It might be expected that the MQSE will result in globally better estimations since it should do better in the regions that were not highly correlated with one of the estimator locations. However, the down side is that it requires full-field measurements or an extensive experimental effort to build up the kernel for the POD. However, if we choose to limit our viewing area to regions that have high correlation levels with the surface pressure, such as near the aft wall of the cavity using point-wise measurements; the QSE should yield better results.

3 Experimental Facilities and Techniques

The work that was conducted for this grant was performed in two newly constructed facilities at the University of Mississippi. The first of the two facilities was designed to study cavities in low-speed incompressible flow conditions, while the second is designed to study cavities of similar aspect ratios in compressible flow conditions. Each of these facilities along with details of some of the instrumentation will be described below.

3.1 Low-Speed Wind Tunnel

The wind tunnel facility is capable of obtaining free stream flow speeds of up to 75 m/s and can be seen in Figure 1. Complete details of the design and construction of the subsonic facility can be found in Murray (2003), hence only the relevant details are included here. The test section's open area measures 0.3 m tall by 0.15 m wide and is 0.6 m in length. A wide variety of cavity length/depth ratios can be tested by placing inserts into an opening below the test section. (See Figure 1)

Fiberglass was placed in the test section ceiling to reduce standing waves associated with the test section height. A slit down the center of the fiber-glass allowed a light sheet to be passed through the ceiling during PIV experiments. Pressure spectra from measurements inside the cavity were analyzed to show that the fiberglass insert was effective at eliminating tones associated with the test section height. These measurements also showed the acoustic treatment did not introduce any new noise associated with the semi-porous surface or the slit for optical access.

The boundary layer was tripped approximately 0.15 m upstream of the cavity leading edge to create a fully turbulent boundary layer with a height of 9.4 mm, for a free stream velocity of 68 m/s. With these conditions the momentum thickness was calculated to be 1.3 mm. Details of the boundary layer profile and momentum thickness calculation can be found in Murray and Ukeiley (2004). Initially, various cavity length/depth ratios were tested to ascertain resonant conditions. These tests were all conducted with a free stream flow of 68 m/s. Figure 2 shows the pressure spectra measured using a single

transducer located in the downstream cavity wall at a distance of 6.35 mm below the cavity mouth. The magnitude is relative, and the configuration ratios are shown in the legend. The two cavity configurations chosen for further study are denoted by an asterisk. The cavities which exhibited resonance in the spectra in Figure 2 yield reasonable agreement with both Rossiter's empirical formula and the results published by Block (1976). The fact that the l/d=5.16 did not exhibit resonant conditions was quite surprising since it satisfies many of the previously proposed criterion for a cavity to exhibit resonant phenomena. However, the focus of the present work is not on resonance parameterization (see Grace et al (2004) for a recent discussion of resonating versus non-resonating cavities); hence these results are presented merely to state the test conditions and the capability of the experimental facility.
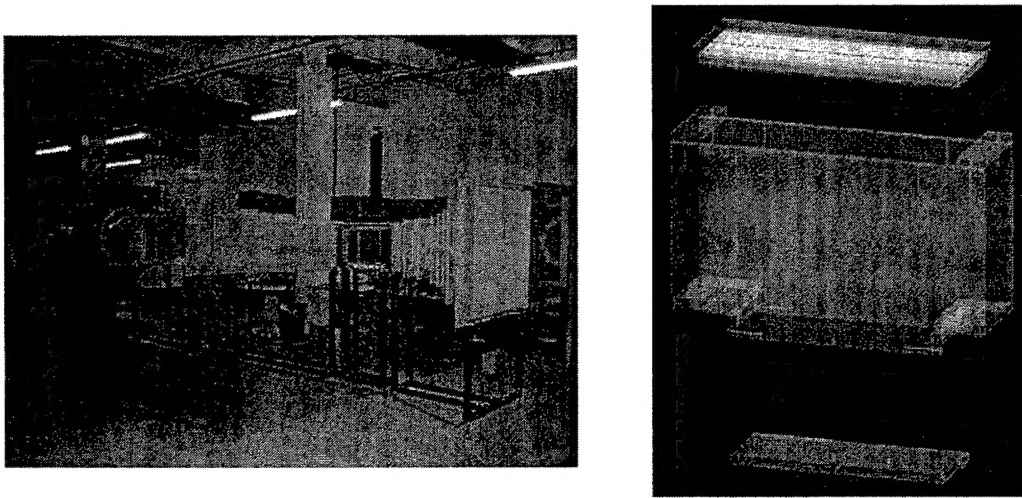
Figure 1: Wind tunnel and test section layout
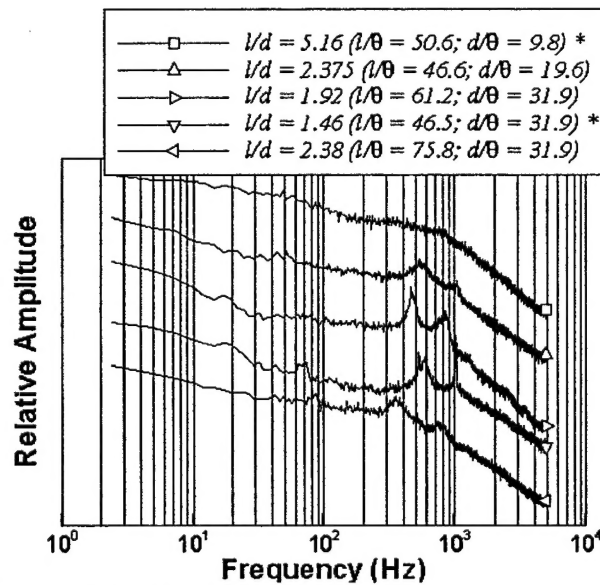
Figure 2: Aft wall pressure spectra Mach 0.2

Two different cavity configurations were chosen for examination in the current study. In both cases the free stream flow speed was approximately Mach 0.2. The shallow cavity was 75.7 mm long and 14.7 mm deep for a length/depth (l/d) ratio of 5.16. As shown in Figure 2 this cavity did not exhibit a resonant peak in the pressure spectra. The deep cavity was 61.7 mm long and 41.4 mm deep giving l/d = 1.49. It should be noted that throughout this work we will refer to the l/d=1.49 cavity as the deep cavity although classically in the literature deep cavities are typically considered to be ones with l/d < 1. Here we are simply using it as a relative term to signify the deeper of the two cavities studied. Rossiter's empirical formula (equation 1) yields frequencies of 430 and 1003 Hz for the first two modes. From Figure 2, the spectrum for this cavity includes a peak at nearly 1 kHz. There is also a broader peak centered around 580 Hz. The 1 kHz tone corresponds to the second Rossiter mode, but the 580 Hz broadband noise does not correspond to the first Rossiter mode. This discrepancy has been documented for low-speed flows over cavities by Block (1976). In that work, results for the l/d ratios and flow speeds used in this study are published and agree with the results shown in figure 2.
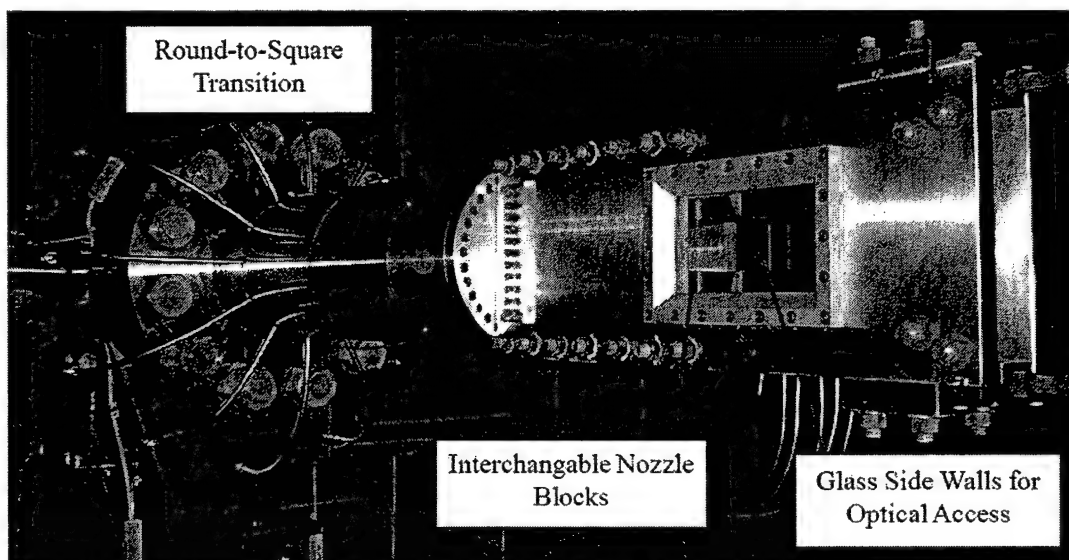

Figure 3: 2-inch Tunnel Facility at the National Center for Physical Acoustics

3.2 2" Compressible Flow Facility

New test sections inserts were built for the 2-inch facility at the National Center for Physical Acoustics. The existing tunnel featured a 2-inch square test section. The facility incorporates interchangeable nozzle blocks to allow testing over a wide range of subsonic and supersonic Mach numbers up to Mach 5. Optical access is available via glass side walls. Figure 3 shows the 2-inch tunnel installed in the anechoic room.

Measurement of the boundary layer thickness at the entrance to the test section showed a thickness of 0.06" at Mach 0.85. Figure 4 and Figure 5 show details of the cavity model test section inserts for the 2-inch tunnel. Figure 4 details the cavity model which was design with a movable rear wall to allow length-to-depth (L/D) ratios from 6 to 9 to be tested. The model includes 10 pressure measurement locations (at L/D = 6; 13

are available at L/D = 9) along the center line. Figure 5 details the test section ceiling which incorporates optical access for a laser sheet to facilitate PIV measurements of the velocity field. The ceiling also includes an acoustic damping material to eliminate refection of acoustic waves.

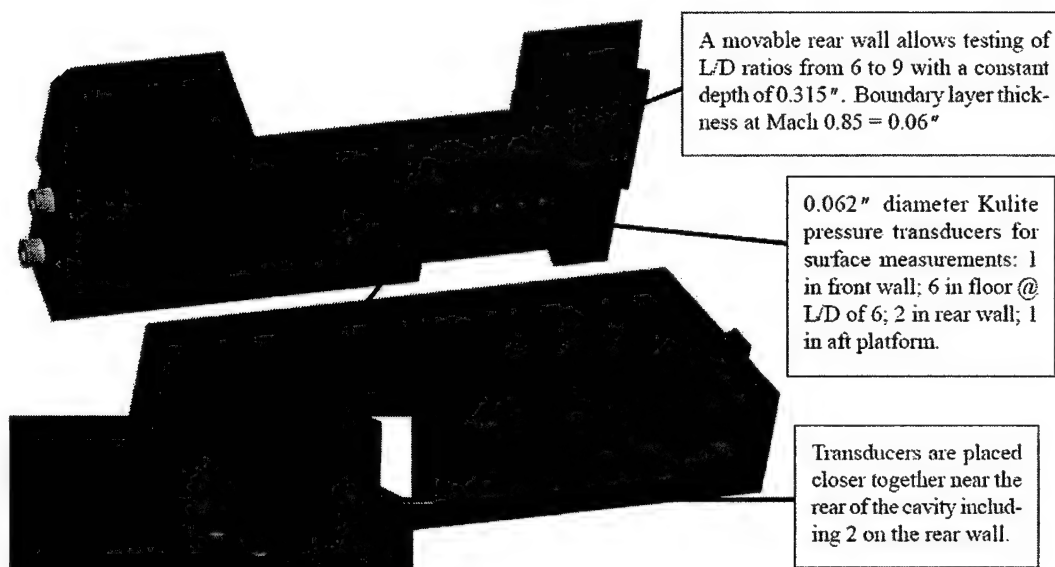The cavity used in these experiments was 0.315" deep, 1.89" long, and spans to the 2-inch width of the wind tunnel.

A movable rear wall allows testing of L/D ratios from 6 to 9 with a constant depth of 0.315". Boundary layer thickness at Mach 0.85 = 0.06"

0.062" diameter Kulite pressure transducers for surface measurements: 1 in front wall; 6 in floor @ L/D of 6; 2 in rear wall; 1 in aft platform.

Transducers are placed closer together near the rear of the cavity including 2 on the rear wall.

Figure 4: Solid Model of Cavity for 2 inch Tunnel

A window provides optical access for PIV measurements.

A porous surface encloses a 1" thick piece of Solimide acoustic damping material.
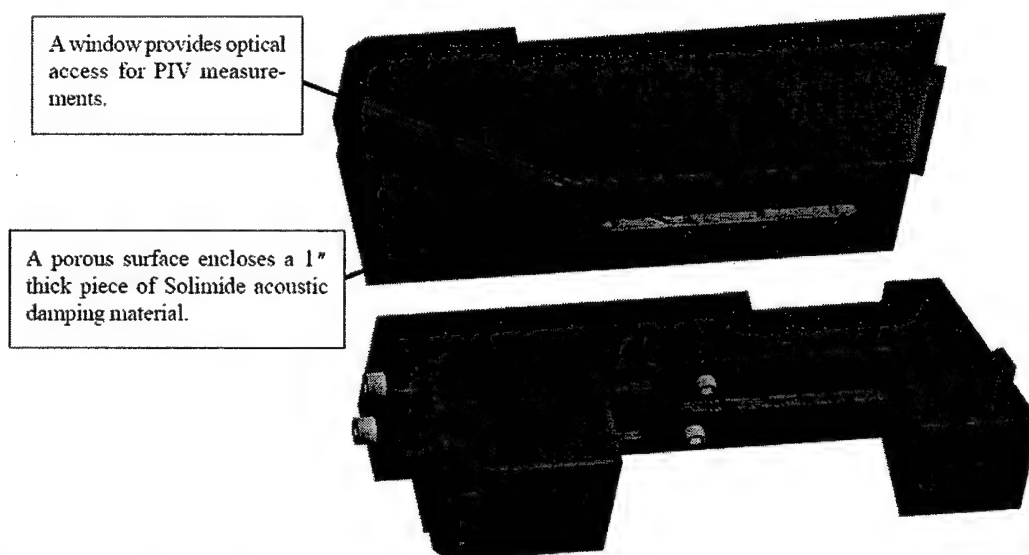
Figure 5: Solid Model of Sound Absorbing Top for 2 inch Tunnel

3.3 Synchronous PIV and Surface Pressure

One of key aspects of this work was the development of the surface pressure based estimation procedure which required the ability to acquire the surface pressure and

velocity field synchronously. Experimental measurements of the velocity/pressure correlations were made using Particle Image Velocimetry (PIV) coupled with surface pressure measurements.

Figure 6 illustrates a typical PIV setup for the cavity flow experiments. This type of setup was employed in both the low speed wind tunnel and the 2-inch tunnel. In both cases, the camera(s) were positioned for 2-D PIV. That is, only the streamwise and vertical components of velocity were measured. The light sheet was created to illuminate a plane normal to the cavity surface and aligned with the streamwise coordinate. For the longer cavities (L/D ratios of 5 to 6) two cameras were used to allow suitable spatial resolution. Figure 1 only shows a single camera for illustration purposes. Collecting PIV images of flows near a surface is difficult due to the reflection of light on the surface. To avoid this issue as much as possible, the axis of the camera lens system was set as close to planar with the cavity surface as possible.
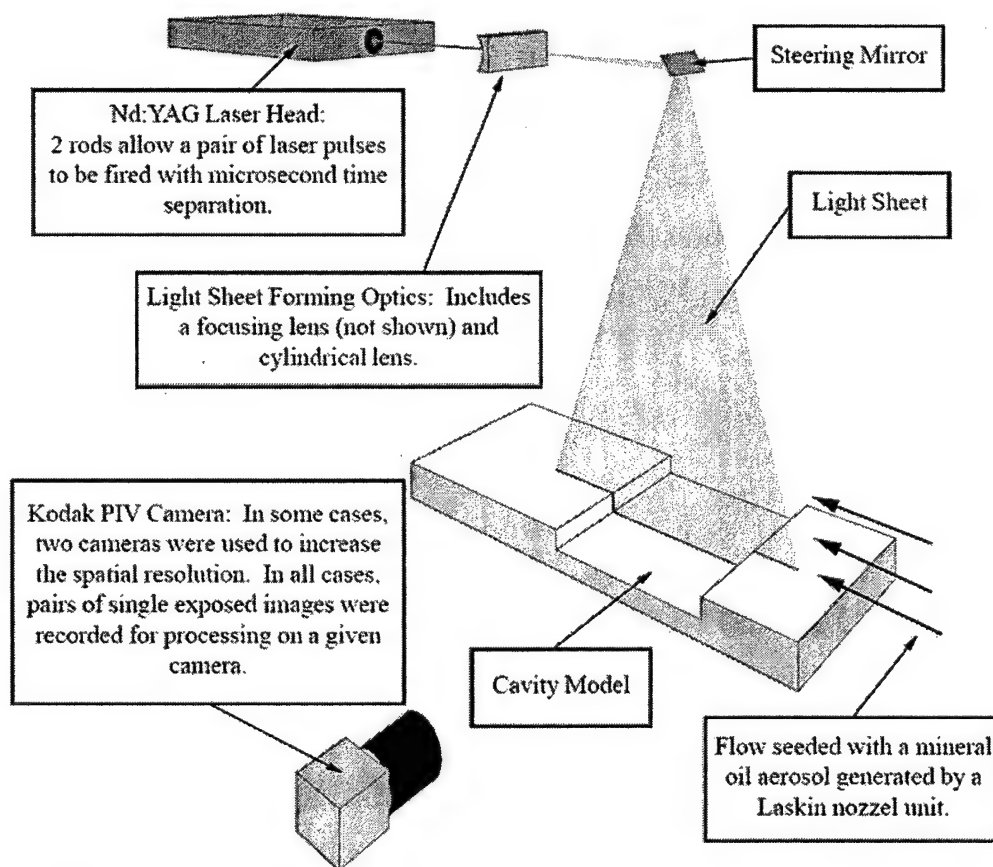
Figure 6: Illustration of 2-D PIV Setup for Evaluation of Cavity Flow

The PIV system utilizes four trigger signals for each individual pair of images. Two "Fire" triggers (one for each laser head) start the charging of the rods. Two "Q-Switch" triggers cause the discharge of the rods. Figure 7 illustrates these trigger signals for a single PIV image pair. The camera's electronic shutter closes at some time between the occurrences of the two Q-Switch triggers, but the shutter is left open for a period

before and after this instant. Therefore, the instant in time corresponding to the collection of an image is determined by the Q-Switch.

In order to correlate the surface pressure measurements with the velocity field, the PIV measurements had to be synchronized with the pressure data collection. This synchronization was performed during post processing by recording the PIV image collection trigger as one of the channels digitized by the A/D system. The sampling rate used to record the pressure data was not high enough to capture the short time separation between Q-Switch's 1 and 2. Therefore, Q-Switch 1 was chosen as the time marker for a given PIV record. Figure 8 shows a small sample of data that displays two representative pressure signals and the PIV image collection trigger (Q-Switch 1). During post processing, the PIV trigger signal would be scanned to find the location of the trigger in the time record. Then, the instantaneous value of the fluctuating pressures at that time would be extracted from the data as the pressure values for the corresponding PIV image pair.

$$\tau_1 = \tau_4 + \tau_2 - \tau_3 \ (\sim 28\mu s)$$
$$\tau_2 = \text{Q-Switch Delay 1} \ (\sim 125\mu s)$$
$$\tau_3 = \text{Q-Switch Delay 2} \ (\sim 115\mu s)$$
$$\tau_4 = \textbf{Pulse Separation} \ (\sim 18\mu s) \textbf{ - This is the actual}$$
time separation between the images within an image pair.
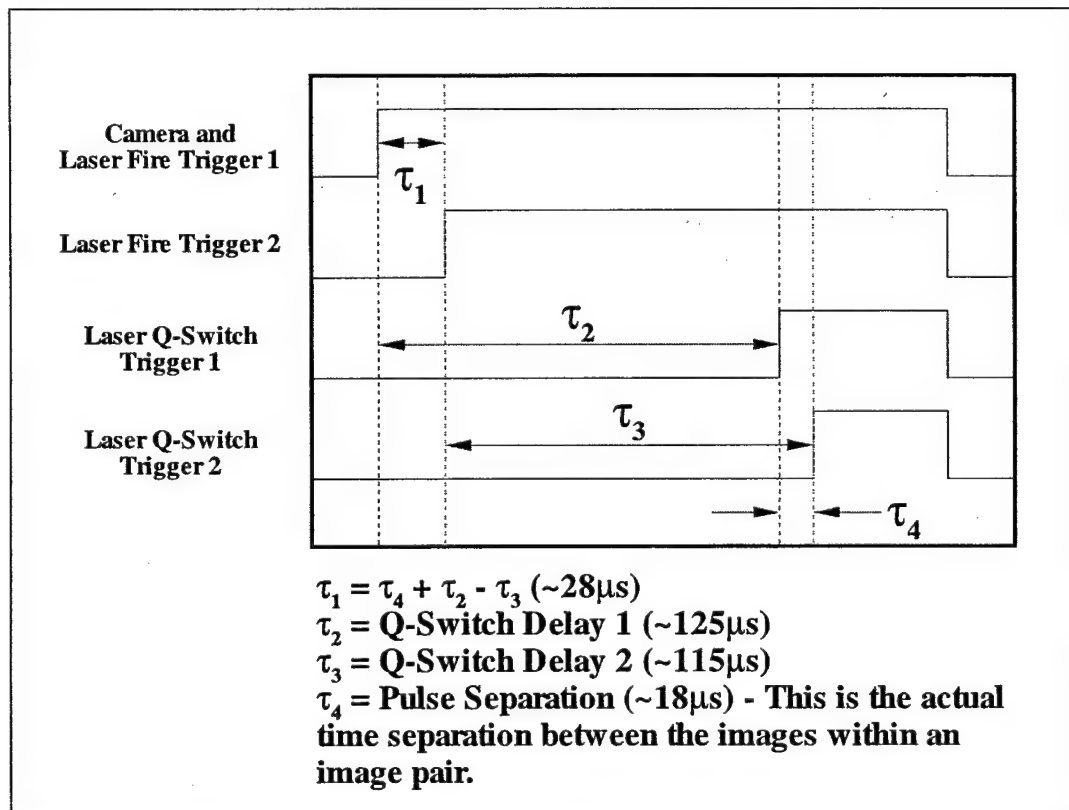
Figure 7: Illustration of the four laser control triggers and the camera trigger that control the acquisition of PIV image pairs. The sequence of pulses repeats for each image pair collected. The time values given are representative values
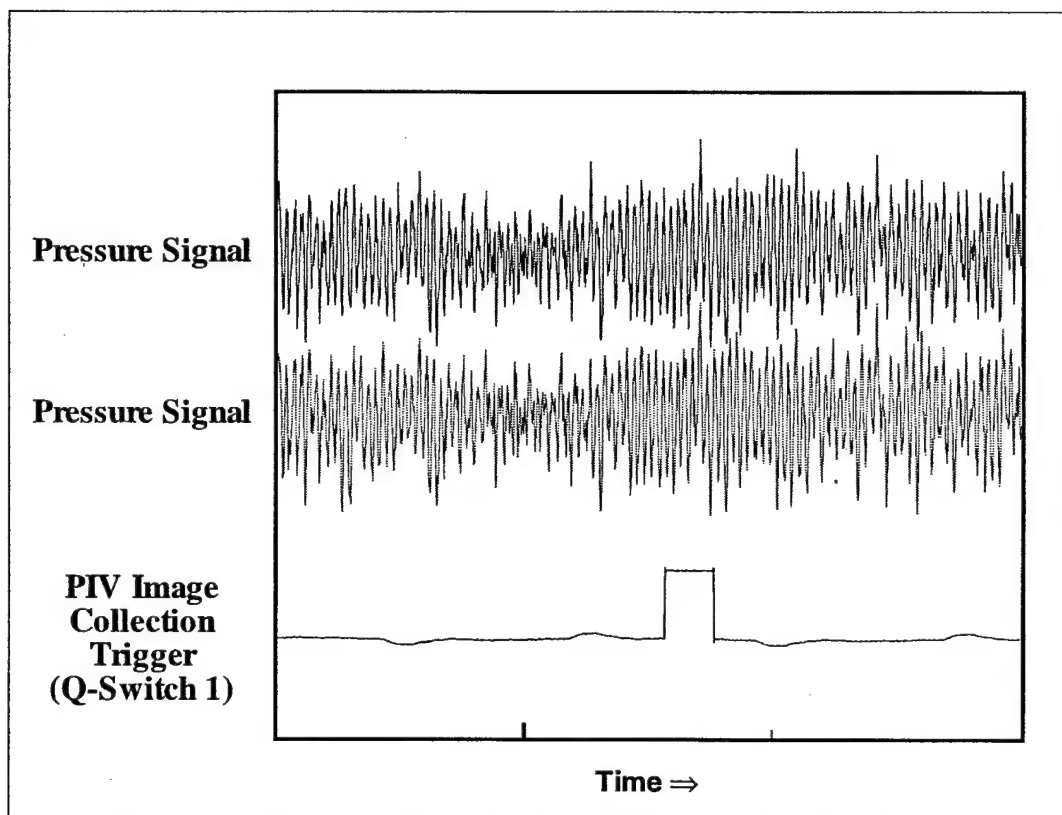
Figure 8: Sample data showing the image acquisition trigger logged along with the pressure data to allow the instantaneous pressure associated with the PIV recording to be collected during post processing.

4 Validation of Stochastic Estimation

In order to evaluate and contrast the capability of the LSE and QSE, the estimations were applied to the data from a time-resolved Navier-Stokes simulation. Information about the simulation that is utilized is presented in section 4.1 along with an explanation of how the simulation results were used to evaluate the estimations. Section 4.2 compares the ability of the two estimates to predict the statistics of the flow. The capability of the estimates to predict the time resolved flow mechanics is also presented in section 4.2.

4.1 Simulation Used For Comparison

To develop and evaluate the stochastic estimation technique, data was analyzed from a Mach 1.5 free stream flow over a cavity with a length to depth ratio of 6. The data set was generated using a Navier-Stokes simulation. Details of the scheme implemented to solve the Navier-Stokes equations utilizing the CRAFT code are provided in Sinha et al. (1991). The CRAFT code has features such as thermochemistry, multi-phase flow capabilities and either subgrid scale or k-ε models to handle turbulent flow. For the data set used here, a large-eddy simulation procedure is used to directly simulate the grid-size scale structures of the turbulence while the subgrid scale dissipative structures are

modeled using a one equation subgrid turbulent kinetic energy (TKE) transport equation. The one equation model of Menon and Kim (1996) is used to solve a transport equation for the TKE which is used to evaluate the eddy viscosity for modeling the unresolved subgrid scale stresses.

Fluctuating wall pressures from the simulation have been shown to agree with Rossiter's formulation. More elaborate details can be found in Sinha et al. (2000). The data set included 192 realizations of the flow sampled at 10 kHz which is sufficient to resolve the time-dependence of the flow mechanics. Evaluation of the estimation based on the simulation data allowed the estimation results to be compared to a standard. The estimation was used to directly recreate the simulation results. The recreation could then be compared with the original to evaluate whether the estimation performed effectively or not. Since the simulation data also included the time resolved flow information, the ability of the estimation to capture the time dependence of the flow could also be evaluated through the same type of comparison.

4.2 Predicting Flow Statistics

One of the keys to the success of stochastic estimation is the strength of the correlation between the estimated quantity and the predictor. If the correlation is low then the estimation will have significant error. Although not shown in this report, examination of the correlation between the surface pressure and the velocity field was used to guide the placement of the estimator locations. Extensive studies of the effects of the location for the estimators were conducted and it was determined that multiple evenly spaced locations along the bottom wall of the cavity yielded the most accurate estimations. The use of multiple estimators also serves to help address issues associated with uniqueness. Obviously there are an infinite number of possibilities in terms of the flow state that could result in a specific surface pressure at any single location on the floor of the cavity. However by using multiple estimator locations which results in coefficients in equation 2-8 being calculated from the correlations between the velocity field and the surface pressure along with the correlations of different surface pressure locations the probability of multiple flow states resulting in that surface pressure signature becomes lower.

Figure 9 shows the estimated RMS velocity field based on an even distribution of 10 points throughout the cavity for both linear and quadratic estimation formulations. The estimator locations are highlighted with the triangles along the cavity surface. As stated above this uniform distribution of estimators was observed to yield the best results. Inspection of the difference between the quadratic and linear estimates in Figure 9 illustrates the fact that the linear part of the estimate captures the bulk of the flow information. Still, overall vector lengths do exhibit a slight increase in the quadratic estimate.

In order to get a more quantitative idea of the quality of the estimation, the rms values were used to calculate streamwise and normal components of turbulent kinetic energy per unit mass for the fluctuating velocities ($E = \frac{1}{2}(u^2 + v^2)$). Figure 10 shows the percent deficit in the energy for the linear and quadratic 10-point estimates as compared to that of the simulated data set. In the figure, an energy deficit of 100% (white color) means that the estimate was unsuccessful at representing the energy in the
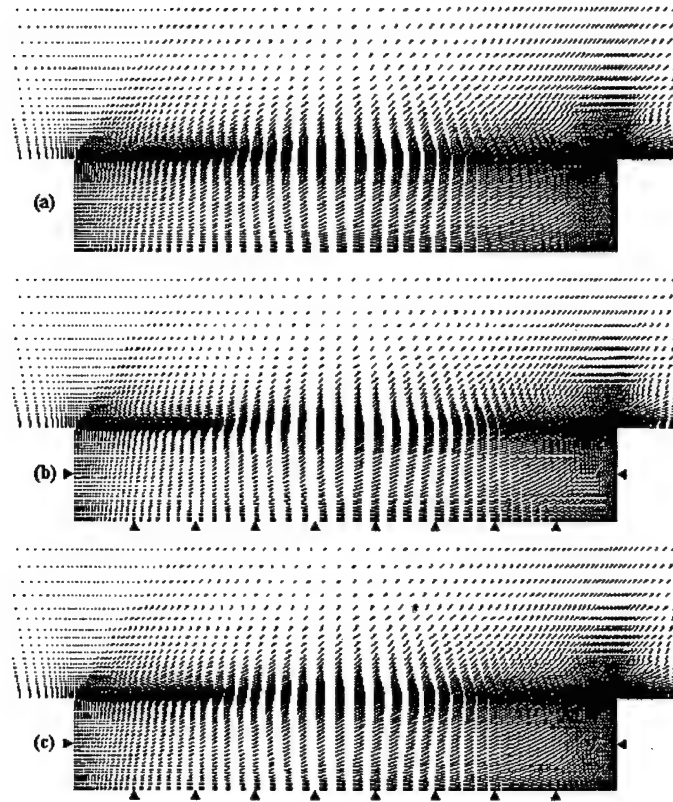
Figure 9: RMS vector plots: a) simulation data, b) 10-point linear estimate, and c) 10-point quadratic estimate
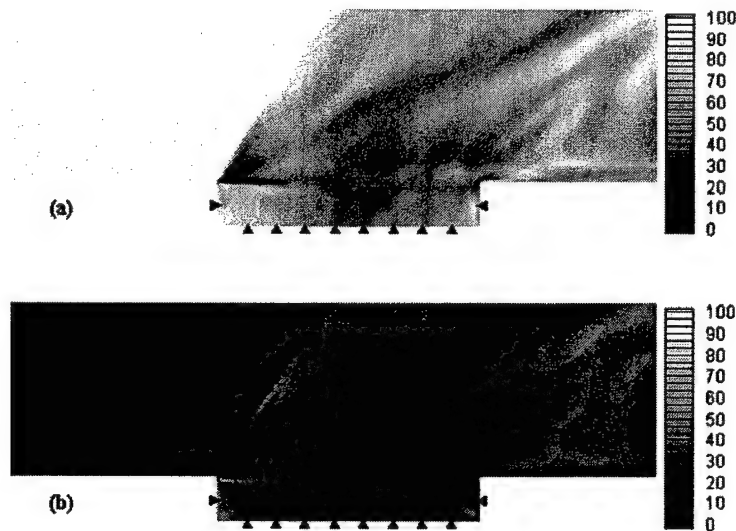

Figure 10: Percent energy deficit: a) linear estimate and b) quadratic estimate

flow. There is a sharp contrast between the quadratic and linear estimate especially upstream of the cavity's leading edge. This shows that the linear estimate is unable to properly represent the integral properties of the flow, especially far away from the estimator location, which is consistent with the results of Naguib et al.

The method of evaluating the rms values of the turbulent velocity gives a good indication of the completeness of the estimate, but it fails to show whether or not the estimate can yield the correct temporal dynamics that will allow for evaluation of the time dependent sources in the shear layer. In order to evaluate the ability of the estimate to produce time-dependent results, the spanwise vorticity was evaluated and compared to the simulation data for successive time steps (1e-4 seconds between time steps). Figure 11 shows seven consecutive realizations of the spanwise vorticity for the Navier-Stokes simulation, the 10-point linear estimate, and the 10-point quadratic estimate. The figure shows the increase in detail gained by including the quadratic term in the estimate. The linear estimate leaves the large structures rather smoothed out. In contrast, the quadratic estimate is better able to represent the changes in the vortex structures. After examining animations of all 192 available time steps, the linear estimate tends to look like a stationary structure that changes shape while the quadratic estimate is able to show the convection and rotation of the structures over time showing the quadratic estimate to be more capable of detailing the evolution of the spanwise vorticity.

The greater detail observed in the quadratic estimate likely stems from the coupling of the pressure measurements in the estimate. The linear estimate is simply a weighted sum of the chosen pressure measurements to produce the estimated velocity. The quadratic estimate includes a weighted 2-point correlation between the chosen pressure measurements. The flow field does not affect individual pressure measurements in an independent fashion, so the inclusion of this "coupling" term between pressure measurements produces an expected improvement and is likely the cause of the enhanced clarity in the quadratic estimated vorticity.
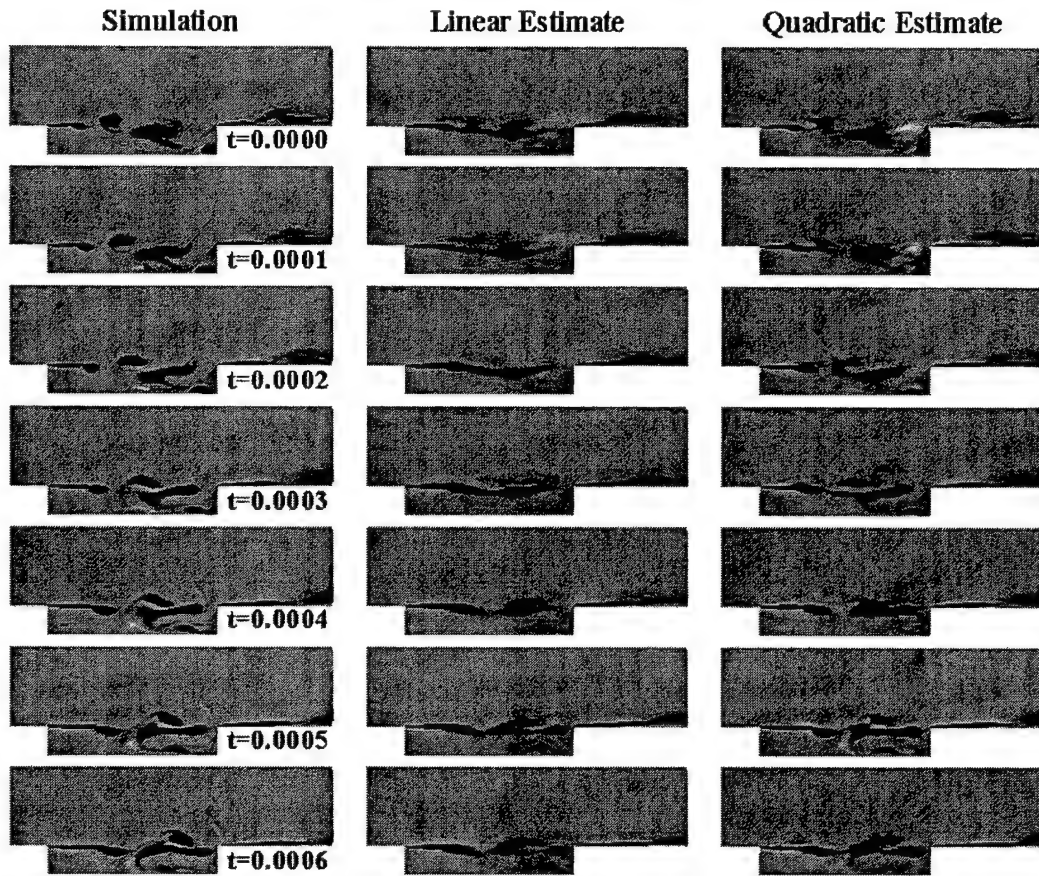
Simulation	Linear Estimate	Quadratic Estimate

Figure 11: Spanwise vorticity for consecutive flow snapshots

4.3 Conclusions Concerning LSE vs. QSE

The preceding observations lead to two very important conclusions. First, the completeness of the stochastic estimate, linear or quadratic, is determined by the correlations included in determining the estimating coefficients. Regions of the flow that are not represented by the correlations will not be properly captured in the estimation. Second, while the linear estimate captures the bulk of the flow information, the addition of the quadratic term is vitally important. This conclusion is evidenced by the observations made in Figure 9 through Figure 11.

5 Cavities in Incompressible Flows

5.1 Flow Field Properties

The mean velocities are displayed in Figure 12 and for the shallow and deep cavities respectively. In all of the figures the fluctuating velocities have been normalized by the appropriate power of the free stream velocity U_o and the spatial directions normalized by the cavity depth, d.
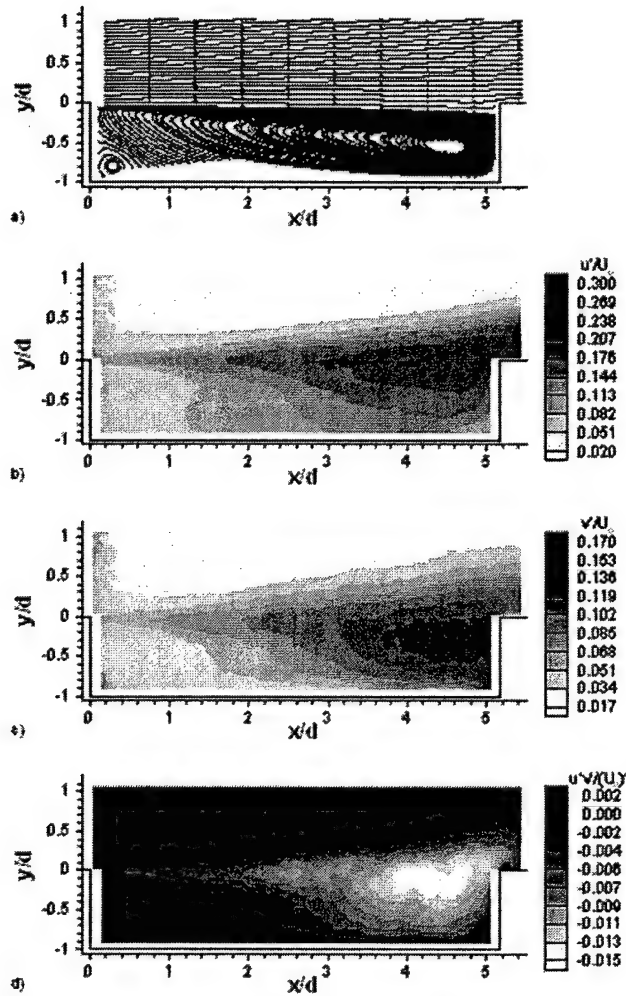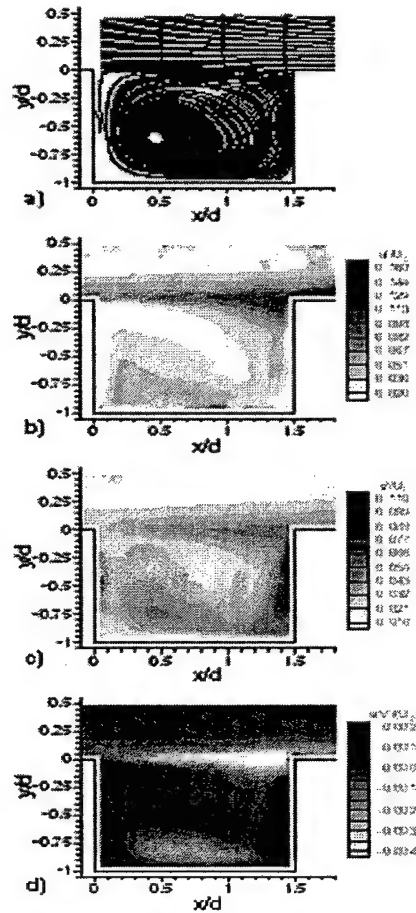
Figure 12: Mean Streamlines and Turbulent Velocities for the Shallow Cavity (l/d =5.16): a) mean streamlines, b) u_0/U_0, c) v_0/U_0, d) $u_0v_0=(U_0)^2$.

The mean flow pattern in the shallow cavity, Figure 12a, clearly displays a recirculation bubble in the rear part of the cavity and a shear layer growing to the point where it nearly spans the whole back wall of the cavity. Examination of the mean recirculation patterns in this cavity shows a large recirculation region that is centered close to the aft wall of the cavity ($x/d=0.85$) and at $y/d=0.5$. The maximum recirculation velocity was found to be nearly 30% of the free stream velocity. In addition there is evidence from the PIV measurements of a smaller counter rotating recirculation region in the front corner of the cavity as one would expect. Detailed examination of the mean flow showed that streamlines from the free stream flow dipped into the cavity and impinged on the aft wall. This happened only in the top 15% of the cavities depth.

The levels of the velocity fluctuations, Figure 12 b and c, are on the order of 25 and 15 percent of the free stream flow for the streamwise and wall normal fluctuating velocities respectively. The shear component of the Reynold's stress, Figure 12 d, are the

same order as the normal velocity, i.e., approximately 15% of the free stream velocity squared. In general the structure of the average turbulent velocities are quite similar for all three components displayed with only a slight shift in the peak location between the streamwise and wall normal components. The structure is predominantly dominated by the shear layer at the cavity opening and the features inside the cavity are at significantly lower levels. However, it is the influence of the vertical component of velocity on the aft wall which shifts the locations of the peak turbulence levels.

Figure 13: Mean Streamlines and Turbulent Velocities for the Deep Cavity (l/d =1.49): a) mean streamlines, b) u_0/U_0, (c) v_0/U_0, (d) $u_0v_0=(U_0)^2$.

For the deep cavity, Figure 13, the mean and turbulent velocities appear to be quite different from those observed with the shallow cavity. The mean flow in the cavity is characterized by a recirculation bubble on the order of the cavity size and nearly resembles a lid driven cavity type flow. Detailed examination of the recirculation bubble showed it being centered in the front third of the cavity, x/d=0.44 and below the vertical centerline, y/d=-0.38. The maximum recirculation velocity is 25% of the free stream velocity. Examination of the streamlines in this cavity showed that streamlines from the free stream do impact the aft wall although only over the top 3% of the cavity. The average velocity fluctuation levels observed in the shear layer of the deep cavity are

smaller than those of the shallower cavity, roughly 14 and 8 percent of the free stream flow respectively for the streamwise and normal velocities. As expected this reduced the shear component of the Reynold's stress in a similar manner. Although the levels of the fluctuating velocity are reduced in the shear layer, both cavities exhibited approximately the same level of anisotropy between the velocity components. Additionally, features of the fluctuating velocity in the cavity, not associated with the shear layer, are also apparent in the deep cavity. These regions of velocity fluctuations can be observed on both the aft wall of the cavity and along the bottom of the cavity and are associated with the large scale recirculation. This as well as the mean velocity clearly shows that this deeper cavity has a large recirculating flow, however, the turbulent energy is much greater with the flow along the aft wall of the cavity and along the floor than it is on the front wall.

Evaluation of the vorticity thickness for both aspect ratio cavities showed approximately linear growth across the cavity and was consistent with the results of Gharib and Roshko (1987) which were consistent with that of turbulent mixing layers. Specifically the rates observed here were dδ/dx = 0.118 and 0.148 for the shallow and deep cavities respectively.
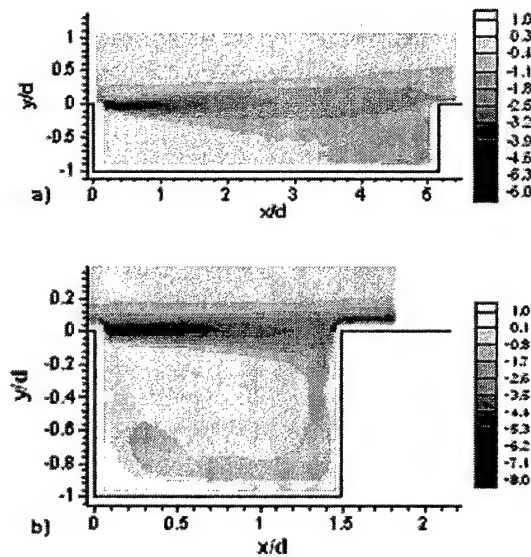
Figure 14: Mean Normalized Vorticity, (ω d)/U, a) l/d=5.16, b) l/d=1.49

Figure 14 displays the normalized mean vorticity which highlights more of the differences between the two cavity aspect ratios. It should be pointed out that the cavity depth has been used for the length scale in the normalization, i.e. (ω d)/U, where ω is the spanwise component of vorticity. For both aspect ratios the mean vorticity is indicative of what was seen with the turbulent velocity fluctuations. In the shallow cavity the vorticity is mostly limited to the shear layer although there are some levels of vorticity that spread throughout the aft section of the cavity. In the deeper cavity the vorticity shows both the shear layer and the large scale recirculation. The peak amplitude of the normalized vorticity is greater in the deep cavity than shallow cavity giving the appearance of higher levels of vorticity. However, the peak amplitude of the non-normalized vorticity is

greater in the shallow cavity implying what is viewed in these plots is an artifact of the length scale chosen in the normalization.

It is puzzling that the non-normalized vorticity magnitude is greater in the shallow cavity which is not resonating. Comparing this to the deep cavity implies that other factors contribute to the strength of the aft-wall noise source which might lead to resonance. One such factor could be the scale of the vorticity related to the size of the aft wall taking into account θ/d and l/d.
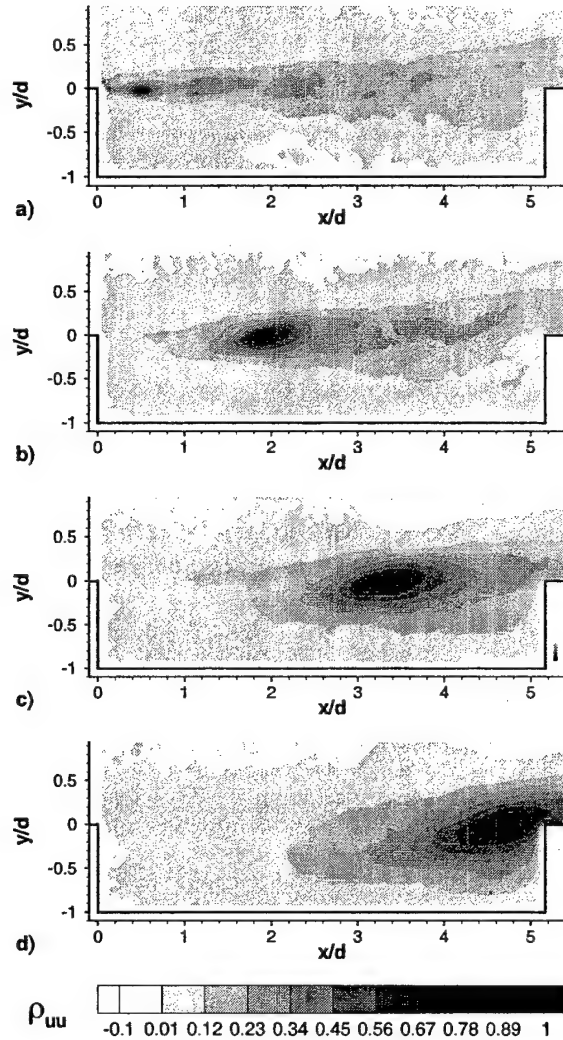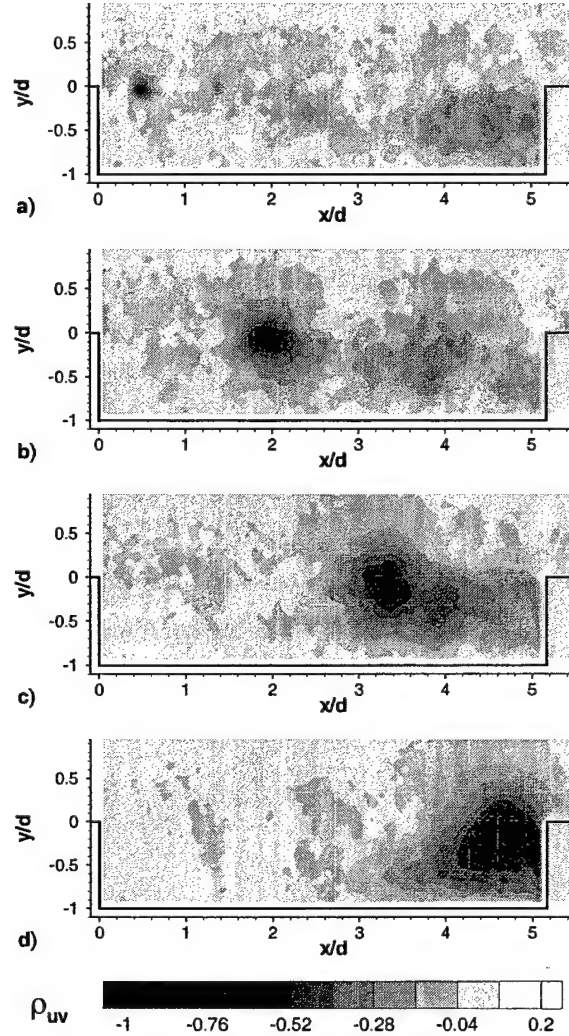

Figure 15: ρ_{uu} Correlations for L/D=5.16 Cavity, (a) Origin = (0.47,-0.03), (b) Origin = (1.88,-0.03), (c) Origin = (3.29,-0.03), (d) Origin = (4.69,-0.03)
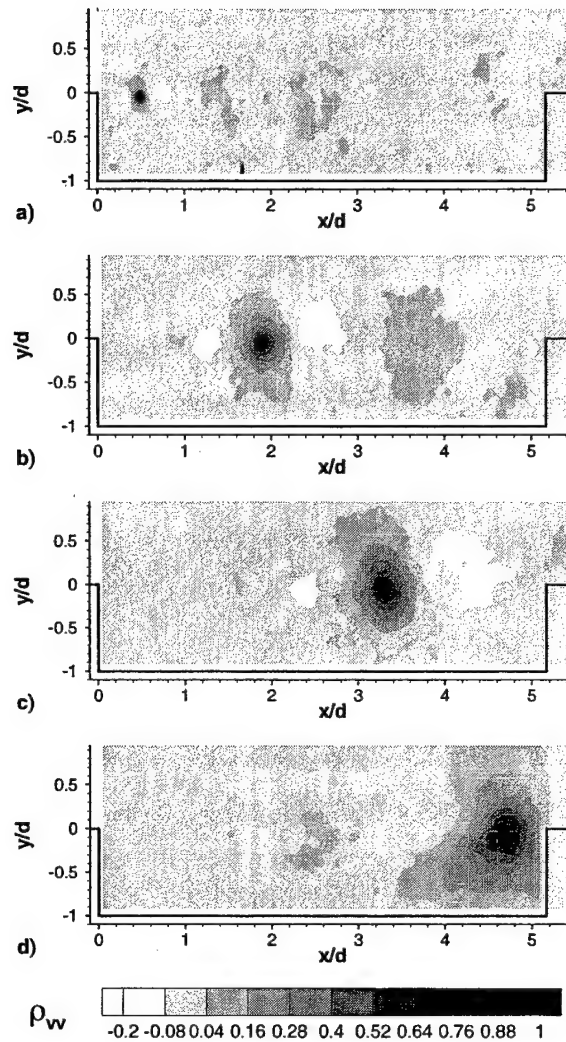
Figure 16: ρ_{vv} Correlations for L/D=5.16 Cavity, (a) Origin = (0.47,-0.03), (b) Origin= (1.88,-0.03), (c) Origin = (3.29,-0.03), (d) Origin = (4.69,-0.03)

Figure 15 through Figure 20 display spatial correlation coefficients for both cavity configurations. In each of the figures there are four graphs which display correlations where the origin is close to the cavity lip line in the vertical direction, $y=d$ ¼ 0, and each one shifted in the positive streamwise direction. The specific origin for each of the plots can be seen in the figure captions. From these plots one can observe the evolution of the spatial scales across the shear layer. Additionally examining the spatial extent of the correlations can also shed light into the noise sources in the shear layer. The largest levels of spatial correlations for the streamwise and radial velocities (figures 9, 10, 12 and 13) for both cavity aspect ratios are limited to the shear layer region for the most part. However, in the deep cavity there does seem to be some weak correlation (coefficients of approximately 0.2) between the fluctuations in the sheer layer and those on the aft wall

and bottom of the cavity. This implies how the recirculation flow is driven by the shear layer across the

Figure 17: ρ_{uv} Correlations for L/D=5.16 Cavity, (a) Origin = (0.47,-0.03), (b) Origin= (1.88,-0.03), (c) Origin = (3.29,-0.03), (d) Origin = (4.69,-0.03)

cavity opening for the l/d=1.49 cavity. In contrast, for the shallow cavity it appears that the only events in the cavity are related to the shear layer dipping into the cavity itself. In both cavities the streamwise velocity correlation is elongated in the streamwise direction while the normal velocity component is stretched in the y-direction. This is expected for a turbulent mixing layer. In fact, the streamwise extent of relatively high correlation levels stretches all the way through the shear layer for origins near the leading edge of the cavity. The general shapes of the correlation areas are quite similar with only slight alterations of the maximum correlation angles. They are in general consistent with what one might expect from a single stream shear layer. However, the vertical scale of the

correlations near the aft wall in relation to the aft wall is quite different for the two cavities. In the shallow cavity the correlation volume spans the entire aft wall while in the
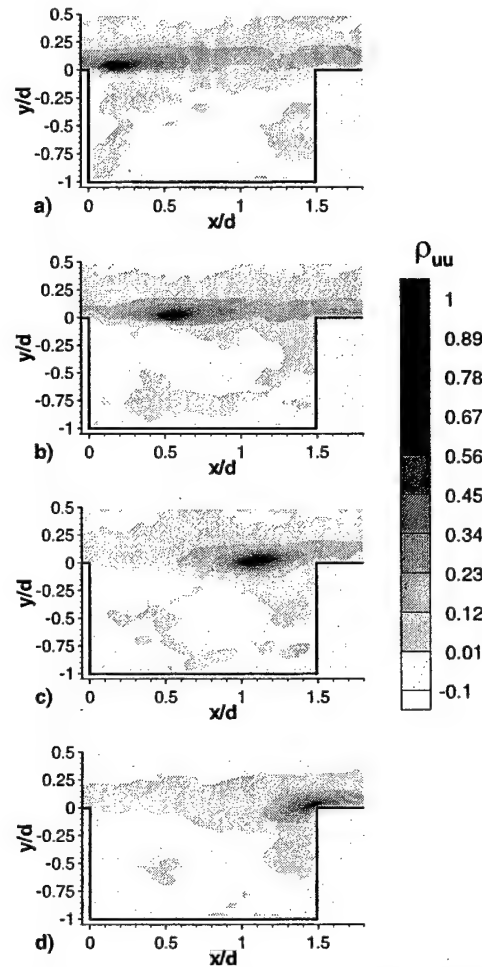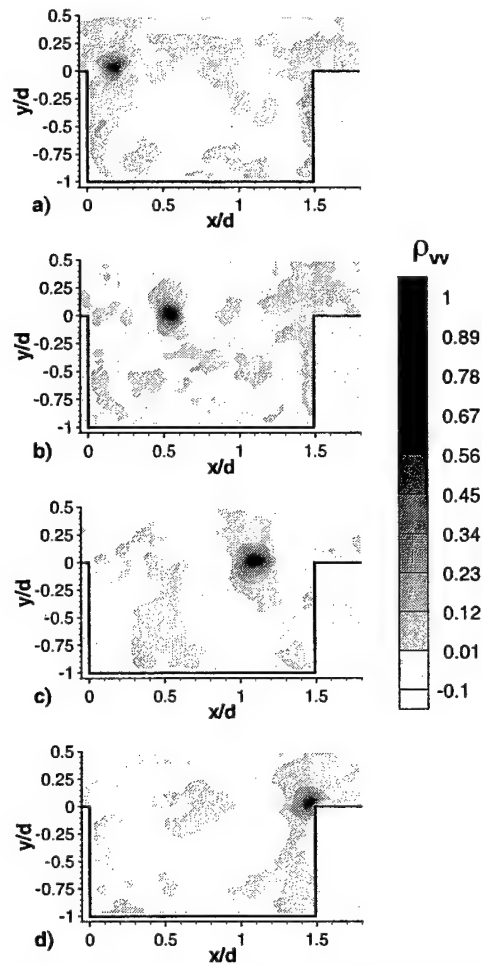

Figure 18 ρ_{uu} Correlations for L/D=1.49 Cavity, (a) Origin = (0.16, 0.03), (b) Origin = (0.54, 0.03), (c) Origin = (1.09, 0.03), (d) Origin = (1.46, 0.03)

deep cavity it is just near the top. This further demonstrates that the growth of the structure of the shear layer does feel the effect of the cavity.

The uv correlations for the two aspect ratio cavities behave differently. In the shallow cavity (Figure 17) it has a behavior essentially the same as the normal component of the velocity field in that it remains restricted to the shear layer region. In the deep cavity (Figure 20) the behavior is different near the cavity walls while in the center of the cavity it has behavior similar to a cross between the streamwise and normal velocity components. Near the cavity walls there is a relatively high correlation coefficient between the streamwise velocity in the shear layer and that up and down the walls. This is indicative of how the recirculation in the cavity is being driven by the streamwise component of velocity in the shear layer. This demonstrates a mechanism for feedback

through the velocity field in the cavity where there is resonance. This mechanics is not apparent in the shallow cavity where resonance was found not to exist.

Figure 19 ρ_{vv} **Correlations for L/D=1.49 Cavity, (a) Origin = (0.16, 0.03), (b) Origin = (0.54, 0.03), (c) Origin = (1.09, 0.03), (d) Origin = (1.46, 0.03)**
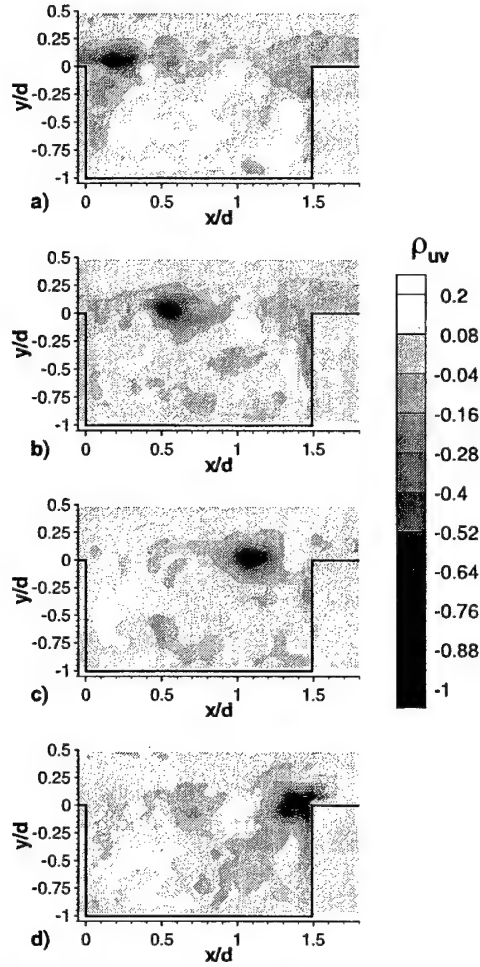
Figure 20: ρ_{uv} Correlations for L/D=1.49 Cavity, (a) Origin = (0.16, 0.03), (b) Origin = (0.54, 0.03), (c) Origin = (1.09, 0.03), (d) Origin = (1.46, 0.03)

5.2 Velocity-Pressure Correlations

Since one of the goals of this work was to use a surface pressure based mean-square estimation technique to study the time dependent velocity, it is important to understand the relationship between these quantities first. In order to better understand how the fluctuating velocities in the shear layer relate to the surface pressure, experiments were conducted by sampling the velocity, with a hot-wire, simultaneously with the surface pressure. The velocity was sampled at the same streamwise locations for both cavity aspect rations. Hot-wire 1 is 45 mm from the downstream wall, and hot-wire 2 is 12.7 mm from the downstream wall. This corresponds to cavity depth normalized streamwise locations of 2.01 and 4.27 for the shallow cavity and 0.38 and 0.8 for the deep cavity. In all cases, the hot-wire probes were at the cavity lip line. Similar results were found for a different vertical location in the shear layer although not presented here. The voltage fluctuations from both the hot-wire and pressure transducers were recorded at a
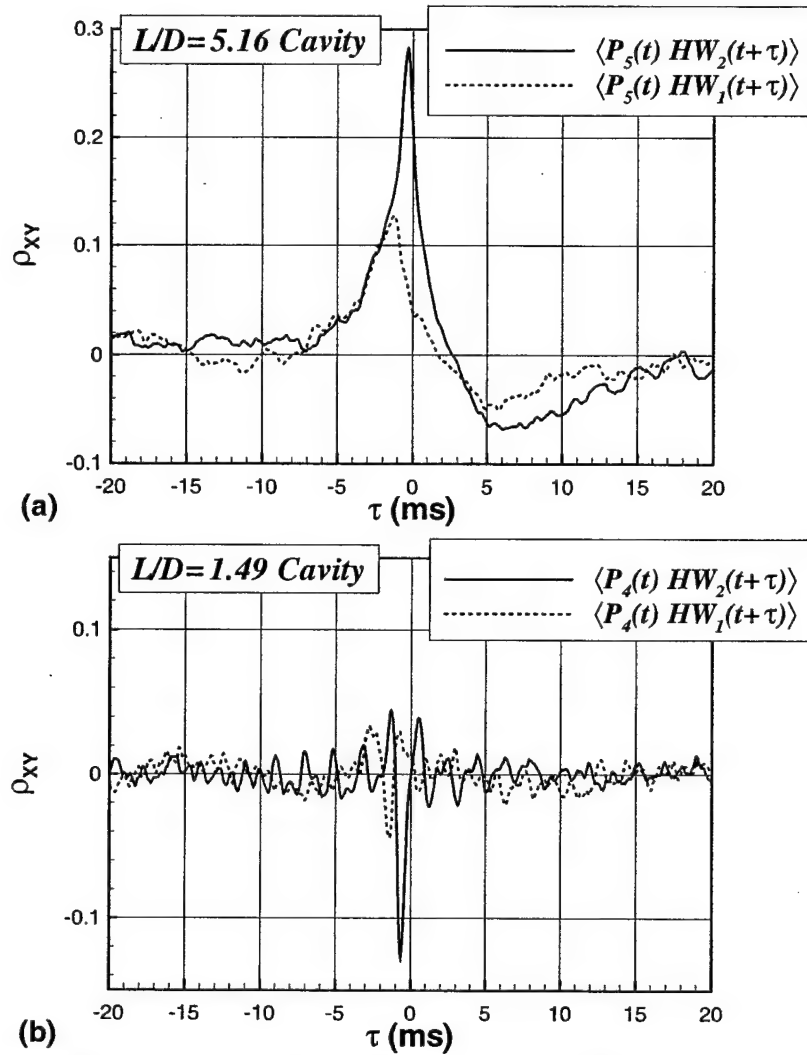
Figure 21: Correlations between Velocity and Aft-Wall Pressure: HW2 location =12.7 mm upstream of aft wall in both cases, HW1 location = 46.0 mm upstream of aft wall in both cases, Vertical location = level with cavity mouth in all cases; (a) l/d = 5.16 cavity, (b) l/d = 1.49 cavity.

30 kHz sample rate giving an uncertainty in time of 16.7 μs. Figure 21 shows the correlation coefficients calculated between the hot-wire measurements and the downstream wall pressure measurement. For which shows that a disturbance detected in the shear layer by the hot-wire is propagated downstream and felt at the aft wall at a later time. Examination of this time lag with regard to the physical distance between the hot-wire and the pressure measurement yields a convection velocity of 38 m/s for other cavity configurations. Compared to the free stream flow of 68 m/s this gives a convective speed ratio of ·= 0.56 which agrees with the measured value reported by Rossiter and that of Murray and Elliot (2001) for a cavity in supersonic flow. Correlation levels for the shallow cavity are obviously larger than those of the deep cavity showing a stronger correlation between the shear layer and the cavity wall pressure. This is partially due to

the location of the pressure transducer in the shallow cavity, i.e., the shear layer directly impacted on the transducer while in the deep cavity the transducer is located below the region where the impact occurs. The trend of higher levels of correlation between the hot-wire measurements and surface pressure for the shallow cavity was found when correlations to the floor mounted pressure transducers were examined. In fact, for the deep cavity, the pressure measurements along the floor showed very little measurable correlation to either of the hot-wire measurements. In contrast, the shallow cavity floor pressure measurements did exhibit measurable correlation levels with the shear layer fluctuations.

The low correlation levels in the deep cavity may have several explanations. First, there is a significantly greater physical distance between sources in the shear layer and the location of the dynamic pressure measurements. Secondly, the feedback path length is increased. Also, the volume of highly correlated fluid is reduced for the deep case which implies that any sources are reduced thus further reducing any direct correlation between noise sources in the shear layer and the cavity surface. However, examination of the correlation between the PIV measurements revealed that there was some level of correlation, although relatively small, between the surface pressure and the velocity for most locations in the shear layer. These low levels are in contrast to similar correlations observed in numerical simulation results of an open cavity in a Mach 1.5 flow as reported in Murray and Ukeiley (2003). This is due to the fact that in the numerical simulations the cavity was dominated by a resonant condition, and the additional noise that is inherent to physical experiments was absent.

5.3 Pressure-Pressure Correlations

To examine the feedback inside the cavity, correlations were calculated between the pressure measurements on the cavity floor. Figure 21 displays the stark contrast between the results for the two cavity configurations.

In the deep cavity, a periodic nature in the correlation suggests the presence of a standing wave inside the cavity. In the shallow cavity there are lower correlation levels and they do not exhibit a periodic nature. Instead, they seem to indicate the signature of the passage of a large scale event traveling downstream in the shear layer. This is seen by examining the maximum value closest to $\tau=0$ and noticing that this maximum occurs for $\tau>0$. This indicates the movement of the pressure associated with the large scale event from $P3$ to $P4$. The results of Rowley, Colonius and Basu (2002) suggest that the acoustic feedback would only be present in cavities which can be classified as in the shear layer mode, implying the deep cavity should be in that classification. This is not the case for the shallow cavity as one might expect after viewing the pressure spectra presented in Figure 2. Comparison of these results to those presented in Ukeiley et al. (2004) for cavities with aspect ratios of 6 and 9 which exhibit resonant phenomena under higher speed flows further upholds the common belief that the aspect ratio is not the correct parameter to determine whether resonance will occur. The cross-spectra were examined extensively for amplitude and phase information although the plots are not included here. It was found that the amplitudes of the cross-spectra were similar for both cavity aspect ratios with the exception of the peak frequencies in the deep cavity where the amplitudes were an order of magnitude higher. Examination of the phase between the
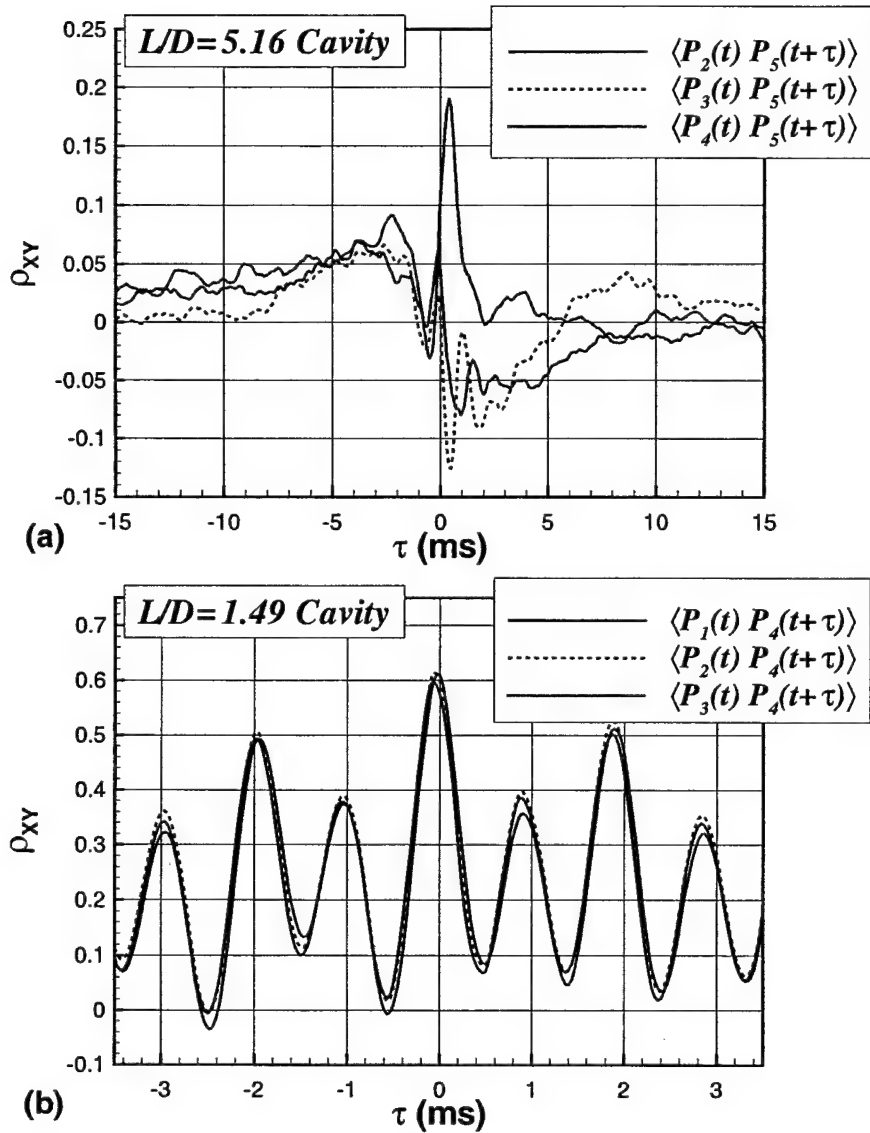
Figure 22: Correlations between Pressure Transducers along Cavity Surface: (a) l/d = 5.16 cavity, (b) l/d =1.49 cavity.

pressure measurements on the floor of the deep cavity revealed that they were in phase at the peak frequencies further implying a standing wave in the deep cavity.

5.4 Quadratic Stochastic Estimation

Using the data collected from the PIV experiment, the quantities on the right hand side of equation 4 were able to be calculated. Then, the time dependence of the shear layer velocity fluctuations was able to be predicted based on the time-dependence of the wall pressure fluctuations. From this, the mechanics of the estimated cavity flow could be evaluated. Figures 15 and 16 show the results for the shallow and deep cavity respectively. The measured wall pressure fluctuations corresponding to each estimated
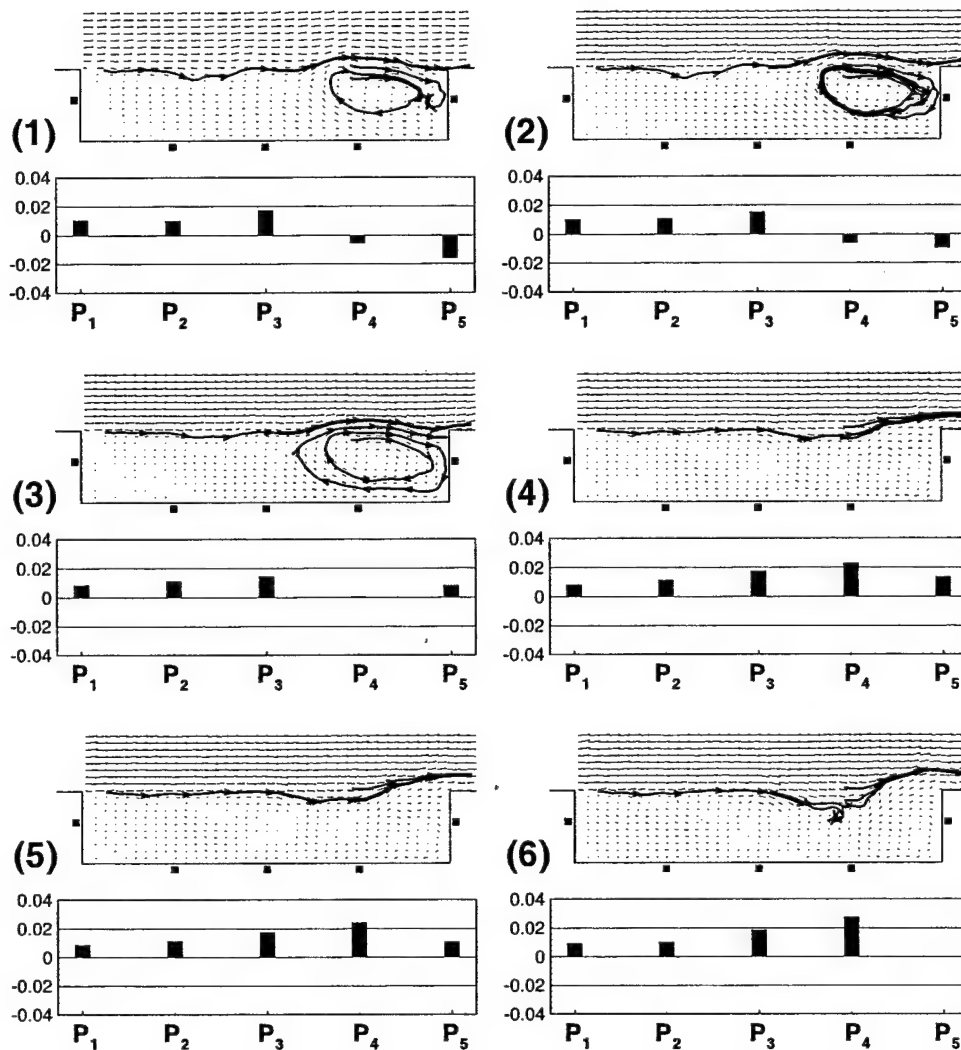
Figure 23: 6 Consecutive Frames of the Estimated Total Velocity in the Shallow Cavity Presented at a Frame Rate of 7500 Hz. Bar Chart Shows Fluctuating Pressure at the Measurement Locations

frame are shown in the bar graph below the velocity map. The pressure value displayed is only the fluctuating part of the pressure and does not include the mean value. In order to create the vector maps in these figures, the QSE output was scaled up to match, in a mean sense, the levels of fluctuation shown in Figure 12 and Figure 13. This scale factor was calculated by comparing the measured turbulent kinetic energy, $\frac{1}{2}((u')^2 + (v')^2)$, to that estimated by the QSE and was found to be 6.13 for the shallow cavity and 7.12 for the deep cavity. It should be noted that this scaling factor was constant throughout the whole spatial domain hence it did not alter the structure of the flow but only the amplitude of the fluctuations relative to the mean. Examination of the spatial structure of the statistical quantities, such as the fluctuating energy, showed excellent agreement
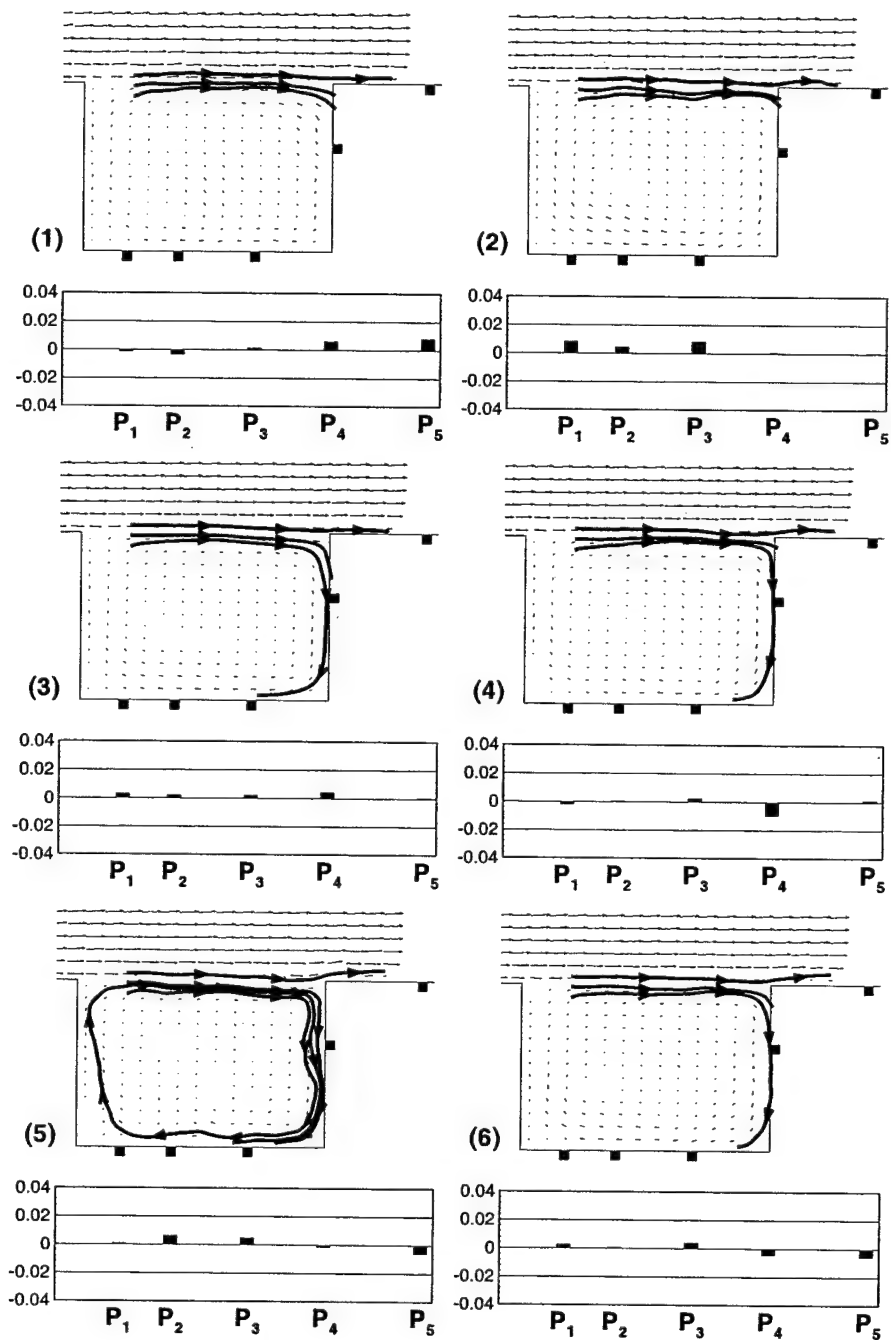
Figure 24: 6 Consecutive Frames of the Estimated Total Velocity in the Deep Cavity Presented at a Frame Rate of 2000 Hz. Bar Chart Shows Fluctuating Pressure at the Measurement Locations

between that measured from PIV and that calculated from the QSE (see Murray and Ukeiley, 2004).

For the shallow cavity, Figure 23, the sequence of frames demonstrates the "pumping" action that occurs in open cavity flows. Frames 1 through 3 show the inhalation phase of the cycle. Then, the cycle shifts to exhalation in frames 4 through 6.

There is a drastic difference in the wall pressures, especially in the downstream sensors, for these two phases of the cycle. The inhalation phase exhibits low or negative pressure fluctuations for the downstream sensors while the exhalation phase corresponds to positive fluctuations. During the inhalation phase there is the formation of a vortex in the aft section of the cavity. This structure then gets ejected during the exhale phase. This observation in the experimental data shows that the large scale shedding and pumping action of the cavity is not necessarily accompanied by a large acoustic resonance (see the lack of discrete peaks in Figure 2).

This cycle is representative of that described in the computational studies of Rowley, Colonius and Basu (2002) in which an initially laminar boundary flow over cavities with similar non-dimensional dimensions at similar free stream flow speeds was studied. Their results detail a flow regime they term wake mode. This flow mode, attributed to the studies of Gharib and Roshko (1987), is characterized by vorticity shed from the leading edge that rolls up and impacts the downstream wall in one part of the cycle and is then exhaled from the cavity in the other part. The present experimental results are similar to this flow mode in the nature of the breathing action at the downstream end of the cavity.

In Murray and Ukeiley (2004), we identified this breathing action as definitive experimental evidence of the existence of the wake mode in a shallow cavity. However, there are several inconsistencies between what is observed here and what has been previously described as features of wake mode oscillations. For example, although there appears to be evidence of the free stream streamlines feeling an adverse pressure, by being bent over the vortical structure in the cavity, in some of the instantaneous flow snapshots the mean free stream streamlines dip into the cavity. The importance of this has to do with separation of the boundary at the leading edge of the cavity which has been deemed important in the previous studies exhibiting wake mode flow. Also, the scale of the vortices being rolled up and shed in the present experiments are quite different from what appeared in the numerical simulations. It appears in their simulations that the shed vortical structures grow to nearly the full length of the cavity while in the present experiments it appears that the behavior is limited to the rear half of the cavity. Furthermore, examination of velocity spectra at points near the aft wall of the cavity exhibited behavior much like the pressure spectra presented in Figure 2, i.e., there was a broad nature with no apparent peaks. This again is somewhat contrary to the numerical simulations where they discuss periodic behavior of the rollup and subsequent ejection.

Given the similar and contrasting characteristics between the experimental results for the shallow cavity and that described for wake mode flow by Rowley, Colonius, and Basu (2002), it is evident that the shallow cavity flow should be characterized as neither a wake mode flow nor a shear-layer mode flow. The lack of any resonance in the pressure spectra or evidence of roll-up in the PIV data or QSE estimation supports the idea that this cavity is stuck in a transitional stage where neither type of flow can sustain itself. This flow might best be characterized as aperiodic, that is, transitional with no resonant oscillations. This notion of begin transitional between wake mode behavior and that similar to flow over a back step without the downstream wall is consistent with Bassioni et al. (2004).

In contrast, the deep cavity, Figure 24, demonstrates a completely different flow regime from what was observed for the shallow cavity. The fluctuations in the shear layer

are smaller, especially near the aft cavity wall, and the recirculation inside the cavity is steady. This is accompanied by lower levels of pressure fluctuations on the floor of the cavity along with a clear peak in the pressure spectra. As discussed in the mean flow results, the shear layer only interacts with the top portion of the aft wall causing the large scale recirculation in the cavity.

Although many features of the dynamical behavior are different from the shallow cavity, the shear layer in the deep cavity still exhibits a pumping action. This action is much less violent than in the shallower cavity but it still exists. Comparing these results to Rowley, Colonius, and Basu (2002), this flow appears to fall into the shear-layer mode regime. In this cavity, streamwise and normal velocity components had peaks in the spectra that correspond to the nearly 1 kHz peak in the aft wall spectra yet the peak around 500 Hz was not apparent. This implies that only the mode associated with Rossiter's longitudinal mode is visible in the velocity field and the other mode is associated with purely acoustics phenomena.

5.5 Summary

There are several important observations that can be made after examining all the results from the various analyses performed. First, the experimental data demonstrates two different modes of cavity flows: One mode is dominated by a shear layer confined to the cavity lid area and an acoustic feedback originating from the aft wall (shear-layer mode). The other mode is dominated by rollup of the shear layer with surface pressure signatures indicative of this structure propagating downstream but lacking any clear resonant tones (aperiodic).

Second, Rowley, Colonius, and Basu (2002) observed shear-layer and wake mode flows under a laminar boundary layer. In the current study, the incoming boundary layer is turbulent. The occurrence of a shear-layer mode under a turbulent boundary layer shows that the presence of a particular mode is not totally dependent on the boundary layer condition. The experimental evidence of two different flow conditions under a turbulent boundary layer is further evidence that the state of the boundary layer may not totally fix the flow mode. However, it is clear that the boundary layer parameters help characterize the resulting behavior. For example, while the two cavity configurations had nearly the same l/θ, which was previously a parameter used to determine the cavity mode, the value of d/θ is totally different between the two cases. In fact, three of the computer runs reported by the above researchers were for $d/\theta = 7.53$ which is very close to the shallow cavity in this case. In all three cases, similar to what was found here, the researchers report no oscillations present. All three computational runs were performed at Mach 0.6 for l/d ratios of 4, 6, and 8.

Another observation involves the relationship between the shallow and deep cavities. In a recent study by Ukeiley, et al. (2004) on the flow over a shallow cavity ($l/d = 5.6$) with free stream Mach numbers of 0.6 and 1.4, the characteristics of shear-layer mode flow were observed similar to the current deep cavity results. These characteristics included a resonant condition and a highly periodic nature in the wall pressure correlations. Therefore, the mode of the flow does not depend on l/d ratio alone. Instead, there seems to be a transition between modes that is dependent on free stream velocity, cavity size, and the size of the boundary layer. This behavior contradicts what has been previously reported since increasing the Mach number and Reynolds number resulted in a

transition from the wake mode to the shear layer mode. This type of behavior further backs statements like that in Grace et al (2004) who claim that parameter ranges specified in studies to characterize cavity flows are only valid when conditions are similar to those where the parameterization was done.

6 Cavity in Transonic Flow

In addition to studying the cavities with incompressible free stream conditions experiments were also conducted in with compressible free stream conditions. These results presented here represent the first set of measurements, surface pressure and velocity, which have been performed in the new 2" tunnel at the NCPA.

6.1 Surface Pressure

6.1.1 Spectra

In order to validate this facility, as well as develop an understanding of properties when different modes are dominant, we examined the surface pressure spectra for a range of free stream conditions ranging from Mach 0.2 through Mach 0.85.
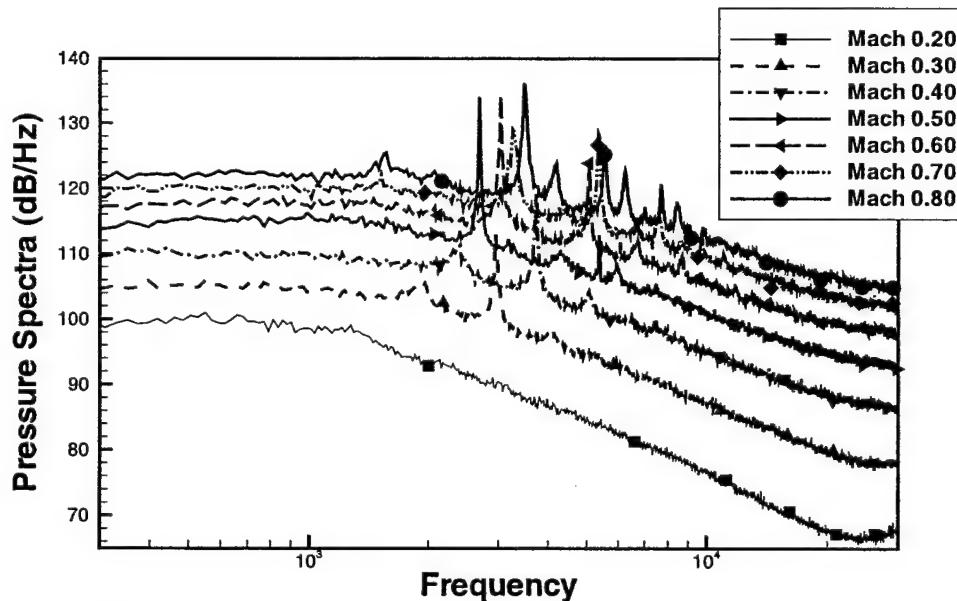
Figure 25: Aft Wall Pressure Spectra in Compressible Flow Facility with L/D=6.0 Cavity

The surface pressure on the aft wall for Mach numbers ranging from Mach 0.2 through 0.8 are displayed in Figure 25. The Mach 0.2 case is quite similar to that measured in the incompressible flow facility which has no discrete tomes and is appears to be dominated by broad band features. The behavior for Mach 0.3 and 0.4 are quite similar where the surface pressure spectra is dominated by a peak close to Rossiters third mode although peaks associated with the second and fourth modes are visible. Rossiter's

second mode was dominant for free stream Mach numbers ranging from Mach 0.5 through 0.8 although at Mach 0.7 the second and third modes are nearly the same amplitude.

One can draw several initial conclusions about the results from this two-dimensional "*small*" cavity. First that the specially designed ceiling worked and the there is no evidence of modes associated with the wind tunnel. Second, the cavity has very similar behavior of the surface pressure spectra to larger cavities experimentally studied, as well as those which have more realistic width to depth ratio. This is **not** to say that there are no three dimensional affects, however the mechanisms that set up resonant conditions predicted by Rossiters theories do exist in a both two and three dimensional cavities. Thirdly, the behavior does evolve with Mach number as has been widely reported.

6.1.2 Cross-Correlations

Cross-Correlation coefficients from the pressure surface measurements for three different free stream Mach numbers along with the location of the sensors are presented in Figure 26. The three free stream Mach numbers represent the three different behaviors displayed by the surface pressure spectra; Mach 0.2 no apparent resonant condition, Mach 0.4 resonance dominated by Rossiters second mode and Mach 0.6 which is resonance dominated by Rossiters third mode. The numbering system used to define the correlations in the rest of this figure are displayed in Figure 26 a.

The behavior observed for the Mach 0.2 free stream condition (Figure 26 b) is different from the two higher free stream Mach numbers as one expect since no resonant peaks appeared in the aft wall spectra, although there are some common features. Even though the surface pressure spectra displayed no resonant peaks, the cross-correlation between the cavities front and aft walls (01, 08) shows a peak for negative time lags which is representative of an upstream traveling wave. The time associated with this peak and length of the cavity corresponds to this peak being representative of a wave traveling upstream at the approximately the local speed of sound. The behavior of the correlation coefficients between the sensors on the floor of the downstream half of the cavity and the aft wall (sensors 5, 6 and 7) have peaks associated with positive time lags which are representative of a downstream traveling wave. The times associated with the peaks in the correlation coefficients correspond to speeds of nearly 0.56 times the free stream velocity. This implies that these sensors are picking up the footprint of the turbulent structures in the shear layer being propagated down stream. Correlations between the aft wall of the cavity and the sensor downstream (08, 10) of the cavity also display a peak associated with an event being convected downstream. One can interpret this as events being ejected at the aft wall then being swept downstream as the flow is re-establishing itself after the cavity.

The surface pressure cross-correlations exhibited similar behavior whether the surface pressure spectra was dominated by Rossiters second mode (Mach 0.4) or third mode (Mach 0.6) as displayed in Figure 26 c and d respectively. For both of these free stream Mach numbers the correlations with the upstream half of the cavity (sensors 1 and 3) exhibited peaks for negative time lags which correspond to acoustic waves traveling upstream in the cavity. For the case where the surface pressure spectra was dominated by
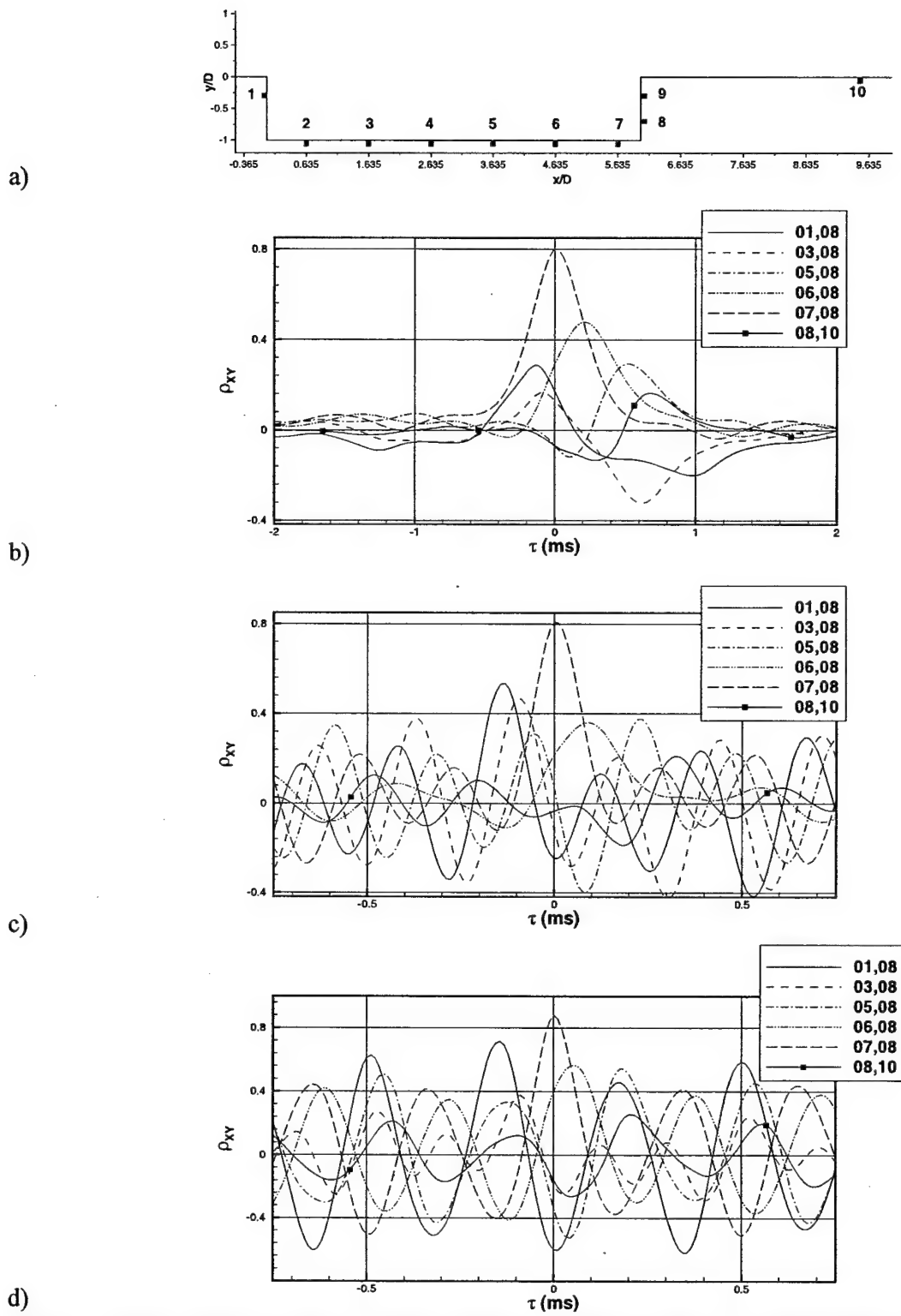
a)

b)

c)

d)

Figure 26: Surface Pressure Cross-Correlations a) Sensor Locations, b) Mach 0.20, c) Mach 0.40, d) Mach 0.60

Rossiters third mode evidence of this acoustic wave was also evident in the surface pressure measurements in the center of the cavity (sensor 5). In the downstream part of the cavity (sensors 6 and 7) the cross-correlations with the aft wall are dominated by a peak for positive time lags, which similarly to the Mach 0.2 free stream case are associated with the foot print of the turbulent structures in the shear layer being convected downstream.

6.2 *Measured Velocity Field*

Detailed PIV measurements were acquired with a free stream Mach number of 0.60. These measurements have been used to analyze details of the velocity field by examining the turbulence properties. In addition we have applied to the Proper Orthogonal Decomposition so that details of the large scale structures could also be studied.

6.2.1 Mean Flow and Turbulent Statistics

The mean streamlines of the cavity flow field are displayed in Figure 27. The mean flow pattern for this Mach number is similar to the shallow cavity examined with the Mach 0.2 free stream flow (Figure 13 a) although there are some differences. In this figure one can clearly see streamlines associated with the mean flow dipping into the cavity and impacting the aft wall. There is also a large recirculating region which is centered two thirds of the way through the cavity in the streamwise direction and halfway in the vertical direction. In general the streamline pattern is more complicated in this higher Mach number flow and more detailed examination is needed to determine the cause.
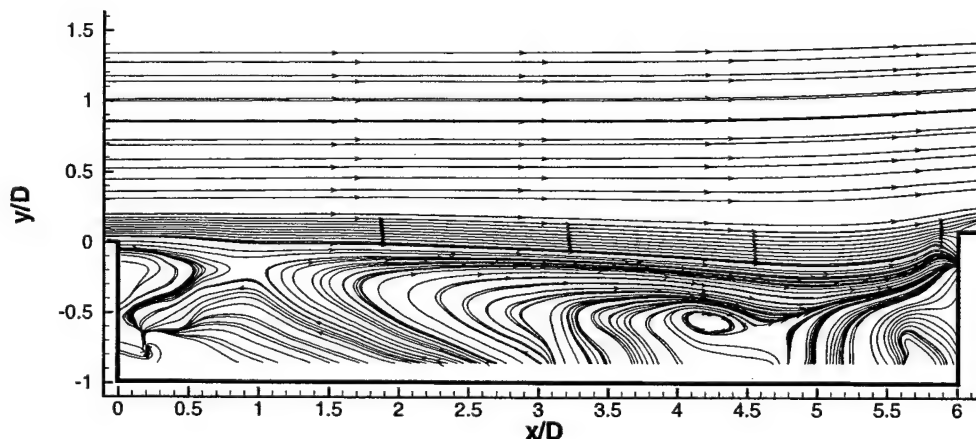
Figure 27: Mean Streamlines of l/D=6.0 Cavity with Mach 0.6 Free Stream Flow

Some of the turbulent statistics for the Mach 0.60 free stream cavity are displayed in Figure 28. Specifically we have plotted the streamwise fluctuating (a), normal fluctuating velocity (b) and the shear component of the Reynolds stress (c). As with the mean flow streamlines there are many similarities with the incompressible flow cavity.

The values of the streamwise component of the fluctuating velocity in the shear layer are on the same order of magnitude as the lower speed case however, for this case there is region of very high levels around the downstream corner of the cavity. The normal component for the rms velocity was nearly identical to the lower speed case in terms of levels and structure. The main difference is a region of high levels of fluctuations near the beginning of the shear layer. The shear component of the Reynolds stress was also quite similar to the lower speed case in structure with amplitudes just slightly higher.

a)

b)

c)
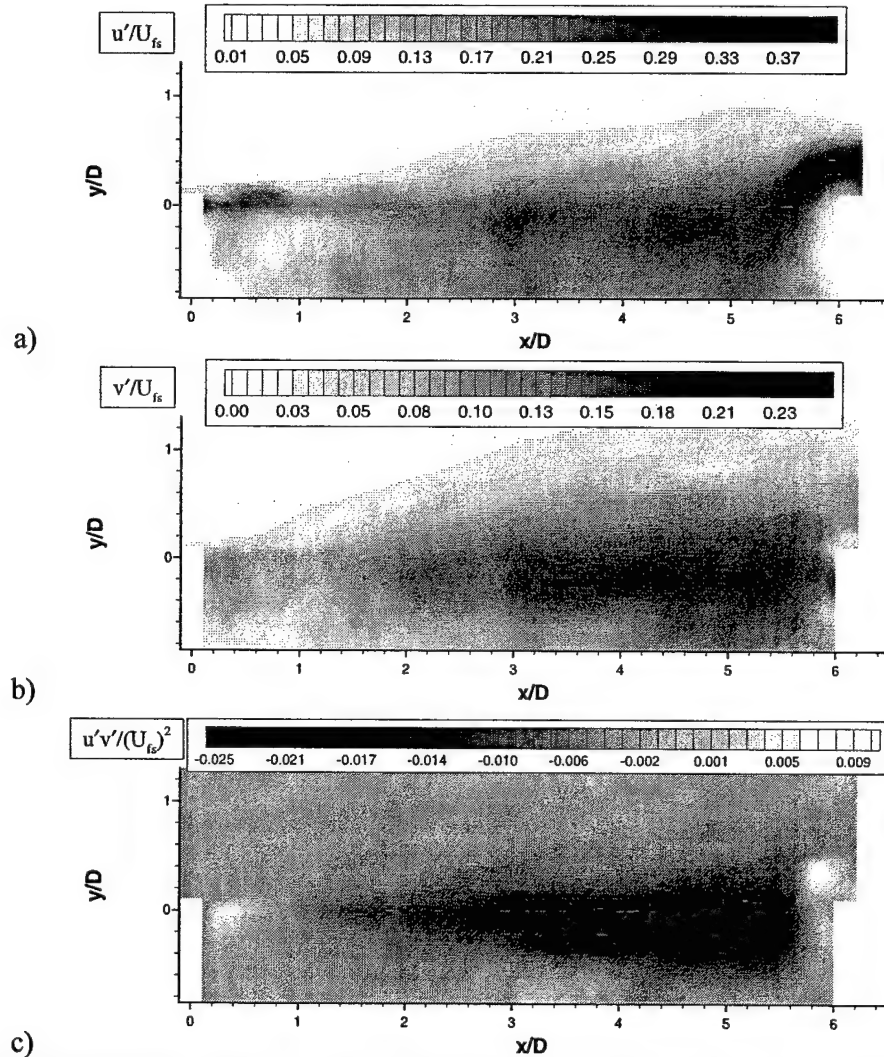
Figure 28: Turbulent Statistics of l/D=6.0 Cavity with Mach 0.6 Free Stream Flow a) u'/U, b) v'/U, c) uv/U²

The fact that the turbulent statistics for the Mach 0.60 case closely mimic the lower speed case, which exhibited no resonant peaks in the surface pressure spectra, implies that the differences in the velocity field might be subtle. Specifically, it appears that the major differences are linked to the kinematics of the of the shear layer and approaches like the ones used here which attempt to develop understanding of the time

dependence of the shear layer are important if one is to understand the fundamental mechanisms creating the broadband surface pressure fluctuations.

6.2.2 POD

Application of the POD to the Mach 0.60 cavity flow field yields insight into the large scale structures. Figure 29 displays the convergence of the energy content of the POD for the two-dimensional application of the snapshot POD. From this plots one observes that the first mode is not overwhelmingly dominant and contains roughly 13% of the overall energy. This is due to applying the POD over the streamwise direction which is only weakly inhomogeneous and is consistent with applications POD to other cavity flow fields; Murray and Ukeiley (2004) to cavities in incompressible flow and Ukeiley et al (2000) to a numerical simulation of a cavity in a Mach 1.5 flow. Although the first mode is not overwhelmingly dominant the convergence of the energy in the POD modes is quite rapid with 90% being represented with only 205 of the modes.
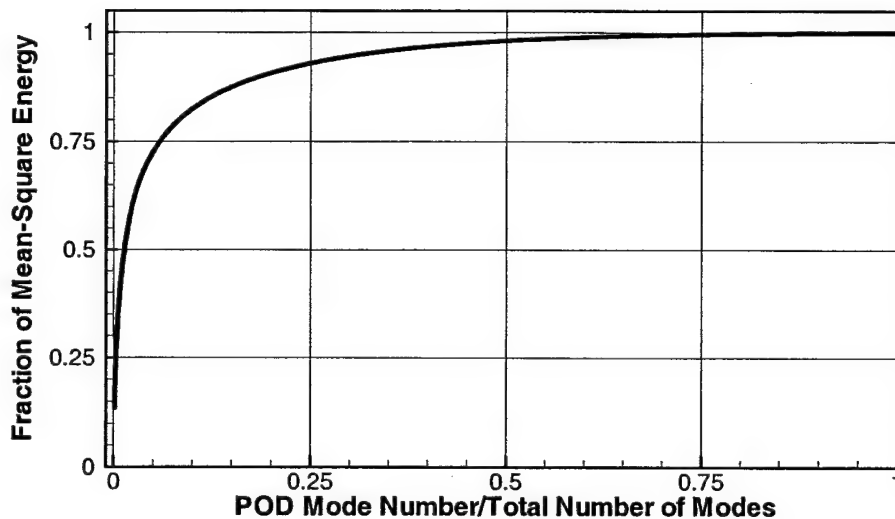
Figure 29: Convergence of POD Modes

The eigenfunctions of the first 9 POD modes are displayed in Figure 30 and Figure 31 for the streamwise and wall normal velocities respectively. In both of these figures the color scheme is such that large positive values are black while large negative values are white. The first mode for both components of velocity highlight the downstream half of the shear layer at the opening of the cavity while the higher modes highlight the more complex modes in the shear layer. This is consistent with other flows where the POD has been applied. Since the POD modes maximize the mean square energy one expects the dominant modes to highlight the area where the turbulent properties are at their maximums.
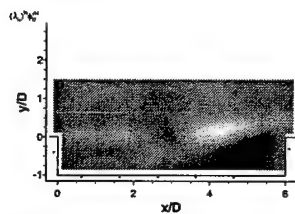
a) Mode 1   b) Mode 2   c) Mode 3

d) Mode 4   e) Model 5   f) Mode 6

g) Mode 7   h) Mode 8   i) Mode 9
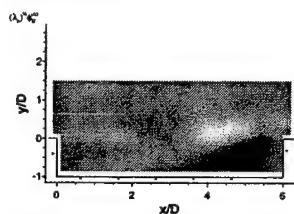
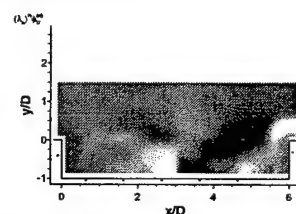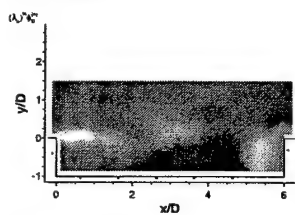**Figure 30: First 9 Streamwise Velocity POD Modes**
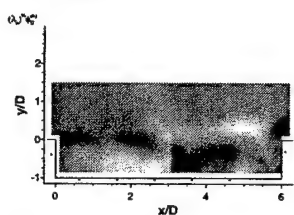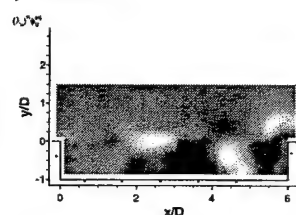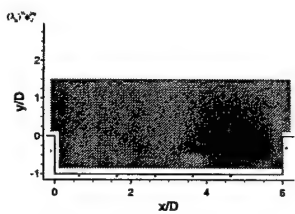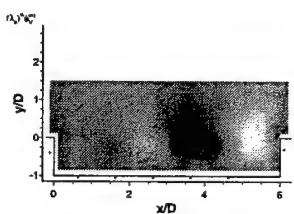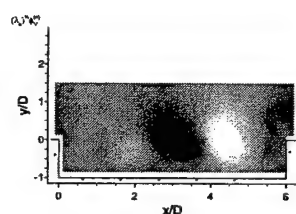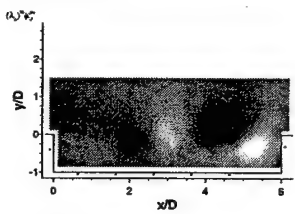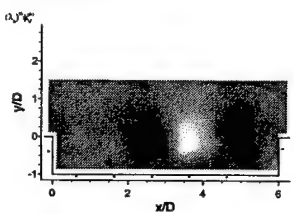
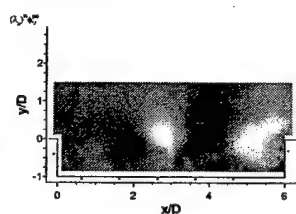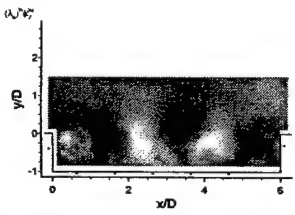a) Mode 1   b) Mode 2   c) Mode 3
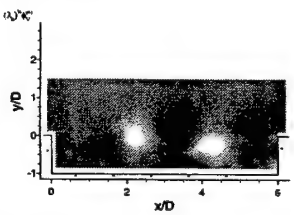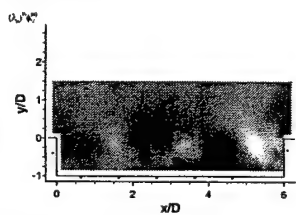
d) Mode 4   e) Mode 5   f) Mode 6

g) Mode 7   h) Mode 8   i) Mode 9

Figure 31: First 9 Normal Velocity POD Modes

From examining the wall normal POD modes the flow structure in the shear layer is clearly evident. Since the POD is applied to fluctuating components of the velocity field a vortical structure is represented by negative region followed by a positive region or visa versa. Specifically, one can see the evidence of flow structure representative of the second and third Rossiter modes in the contour plots presented in Figure 31. POD modes 3 and 4 are representative of the second Rossiter mode and a pair of structures across the cavity opening. While POD modes 7 and 8 appear to be representative of the third Rossiter mode with three structures across the cavity opening.

The evidence of different POD modes being represented of different flow structures known to exist in the shear layer is encouraging for several reasons. Firstly, it shows that although the POD modes are extracted through the maximization of the mean square energy they are representative of the large scale flow features in the flow. Additionally it implies that when low-dimensional models and/or reconstructions are used one should be able to examine different flow modes independently.

6.3 Estimated Velocity Field

The results from estimating the time dependent velocity field using both the QSE and the modified estimation procedure will be presented in this section. For both estimation procedures, first the mean turbulence properties of the estimated field will be presented then a series of time resolved flow snapshots will be used to show the convection of the turbulent structures in the shear layer. In each of these cases the time dependent estimators were seven pressure transducers on the floor of the cavity and will be indicated in the figures.

6.3.1 QSE

The turbulence quantities calculated from the QSE estimated velocity field (equation 2-8) are presented in Figure 32. In general the structure of the turbulence properties is quite similar to those from the PIV measurements, Figure 28. The streamwise rms component has its maximum near the downstream edge of the cavity and has secondary features associated with the broadening shear layer as it evolves in the streamwise direction. The wall normal rms velocity highlights the shear layer similarly to the measured velocity field. The peak values are close to the center of the shear layer and follow close to the
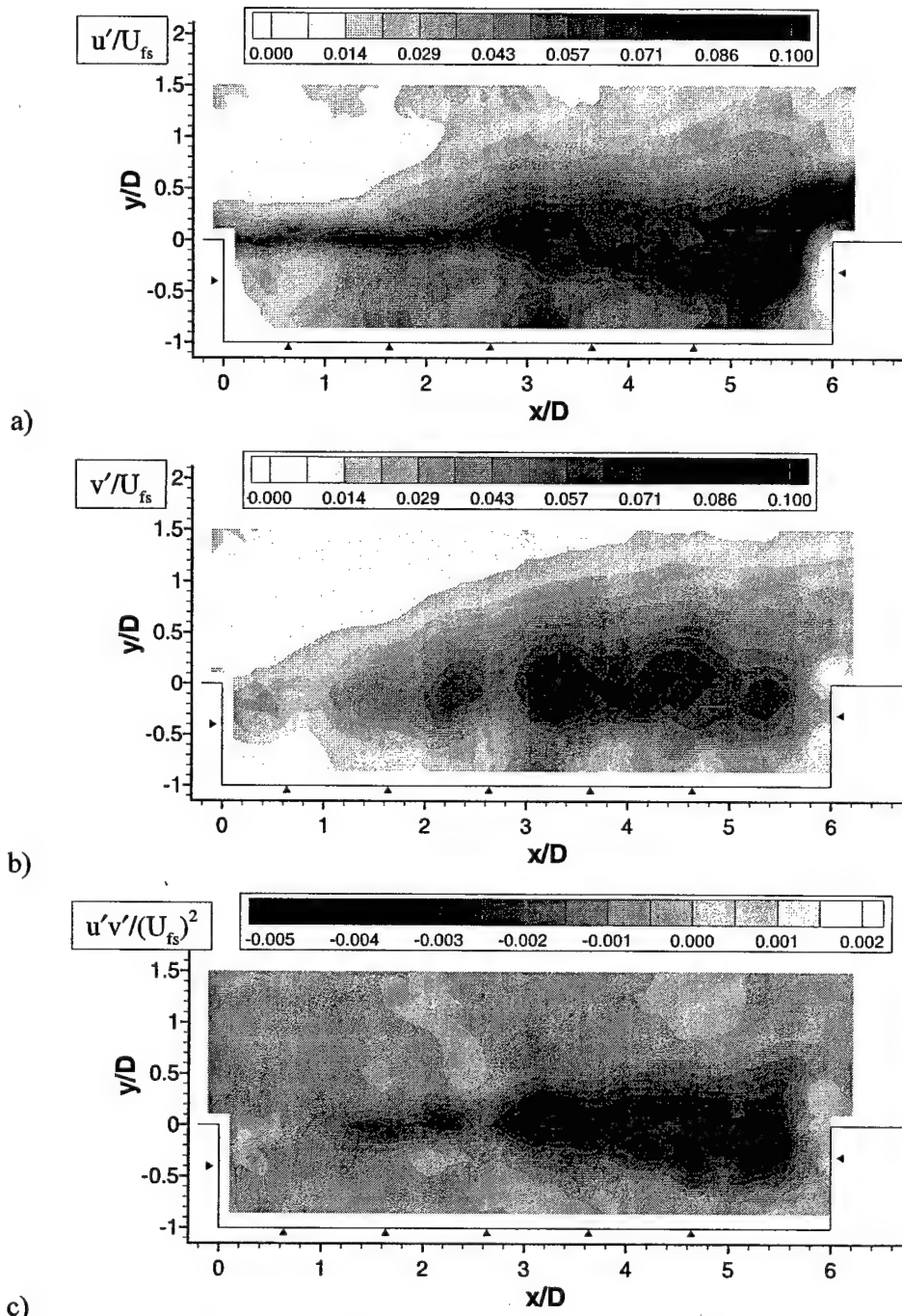
Figure 32: Turbulent Statistics of l/D=6.0 Cavity with Mach 0.6 Free Stream Flow Estimated with the QSE a) u'/U, b) v'/U, c) uv/U²

cavities lip line. The shear component of the Reynold's stress is again quite similar to that measured with the PIV and is predominantly negative in the shear layer. The magnitudes for all of the statistical turbulence properties examined were on the same order as those measured although they were under predicted by nearly a factor of three.
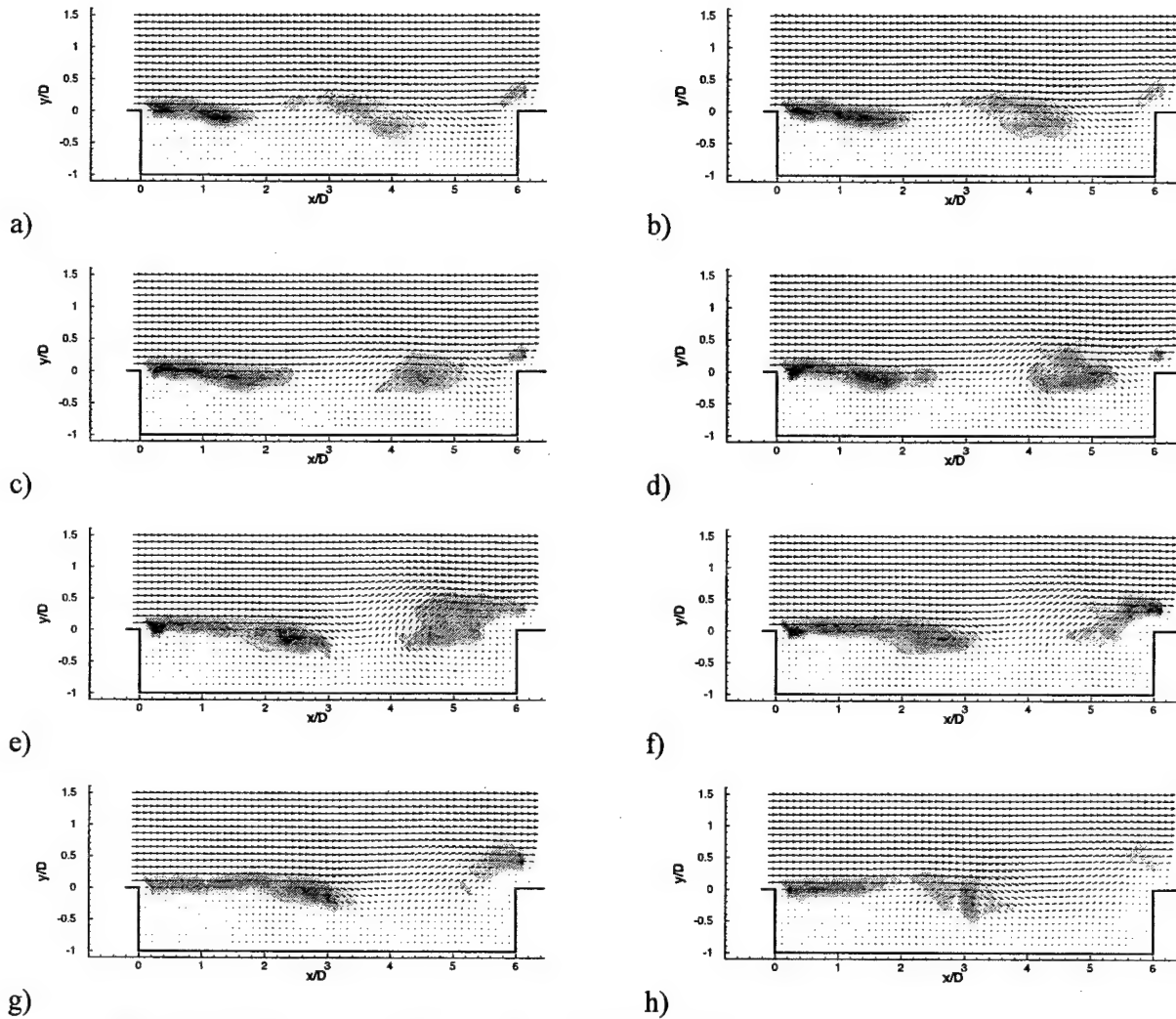
Figure 33: Time Dependent Estimated Velocity Field, δt=66 μsec

Eight sequential snapshots of the estimated velocity field sampled at 15 kHz are presented in Figure 33. It should be reiterated that these velocity fields were estimated from pressure sensors at the 7 locations pointed out in Figure 32. In each of these figures the spanwise component of vorticity is plotted using gray scale contours on top of the velocity vectors. In figure b there is evidence of a vortical structure which was shed from the leading edge of the cavity and rolled up in the first half of the cavity and appears at about x/D=4. In snapshots c, d and e this vortical structure appear to grow as it is convected downstream until it reaches a location just past x/D=5. In snap shots f, g and h the structure interacts with the aft wall and then the vorticity appears to be swept past the cavity onto the floor behind the cavity. Additionally, in these three snapshot one can see the formation of the next structure at approximately x/D=2.5 in snapshot f which then appears to convect downstream in the following snapshots. These snapshots also show

strong evidence of the large amounts of fluid being pushed in and out of the cavity at the aft wall along with several other locations through out the cavity.
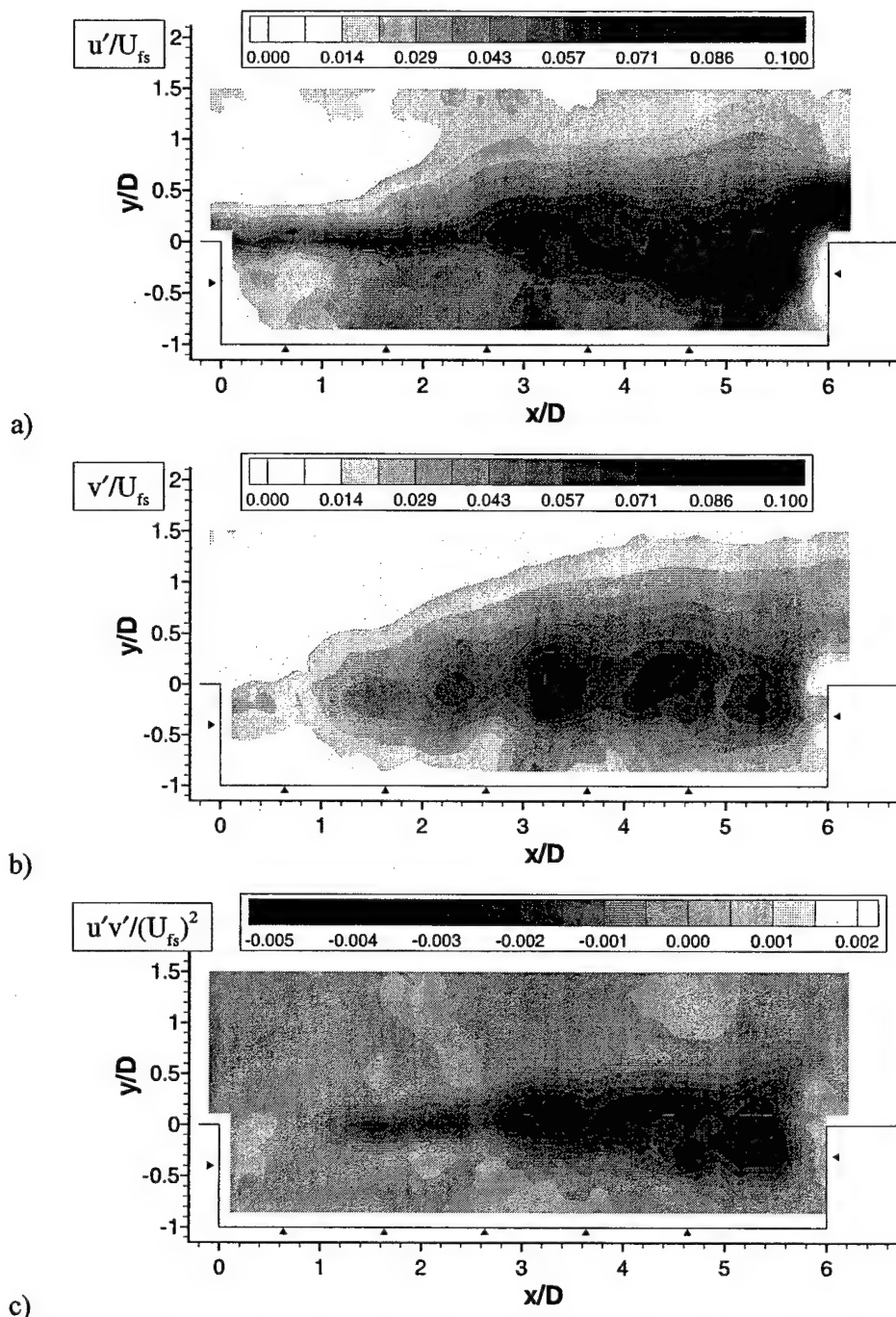

Figure 34: Turbulent Statistics of l/D=6.0 Cavity with Mach 0.6 Free Stream Flow with mQSE a) u'/U, b) v'/U, c) uv/U^2

6.3.2 mQSE

The results from estimating the velocity field using all of the POD modes in the modified stochastic estimation procedure are presented in Figure 34 and Figure 35. These estimates were performed using the same time dependent estimators and are also indicated in Figure 34. In all of the plots presented here equation 2-16 is used to estimate the POD expansion coefficients then equation 2-13 is used to calculate the estimated velocity field and the summation is over all of the POD modes.

The mean turbulent properties, Figure 34, are nearly identical to those of the QSE presented in the last section. This implies that on average there is little difference between the two techniques although the QSE involves estimating each grid point independently and the mQSE involves estimating a single quantity, the POD expansion coefficient.

a)

b)

c)

d)

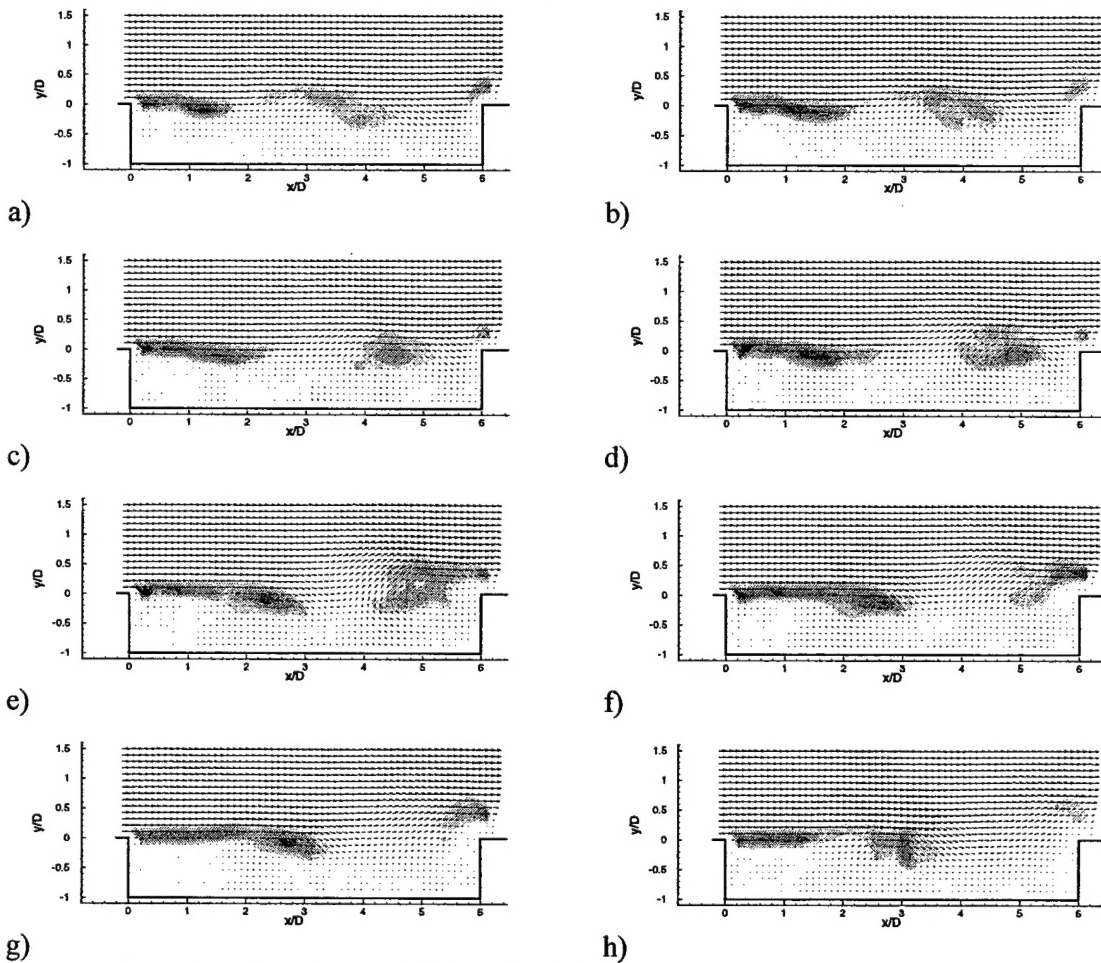e)

f)

g)

h)

Figure 35: Time Dependent Estimated Velocity Field, δt=66 μsec

Figure 35 displays eight sequential snapshots of the flow field using the mQSE technique using the same estimators that were used in the QSE to create Figure 33. As

with the statistical quantities displayed in Figure 34 there is very little difference between the QSE and the mQSE technique when all of the POD modes are used.

7 Summary and Conclusions

The work conducted as part of this grant has lead to several important outcomes. These outcomes include the development of new facilities at the University of Mississippi, development and improvement of techniques to study the dynamics of flow fields and insight into the mechanisms that lead to intense aeroacoustic environment in cavity flows. The detailed flow and surface pressure measurements represent a database that has shed light into the mechanisms governing cavity flows and can be used for continued study. While the estimation procedure has been used to show the first time resolved experimental data showing the evolution of vortical structures in the shear layer above the cavity and how they interact with the aft wall.

The following list summarizes some of the major findings related to the estimation technique and open cavity flows;

- A surface pressure based technique for estimating the velocity field was developed and refined in this work. Validation of the technique using numerical simulations showed the importance of including the quadratic term. Specifically, including this term helped to correctly mimic the dynamics of the structures in the shear layer above the sensors and predict the velocity field far away from sensors. It should be noted that in addition to serving as a way of obtaining time resolved measurements the estimation techniques studied decompose the flow in a way where one can study the large scale structures or other features of the flow independently.
- Estimating the velocity field for a non-resonating cavity (Mach 0.2, L/D=5.16) showed the existence of a strong pumping action. This flow exhibited the rollup of the shear layer but its interaction with the aft wall did not have the energy to sustain the resonant conditions observed at higher free stream speeds.
- Cross-correlations of the surface pressure measurements inside the cavity were shown to reveal evidence of the shear layer structures propagating downstream and of an acoustic wave propagating upstream in cases where resonant phenomena existed. The downstream propagating structures were convected at approximately 56% of the free stream velocity and were there whether the cavity exhibited resonant phenomena or not.
- Estimating the velocity field for a resonating cavity (Mach 0.6, L/D=6.0) clearly showed the large scale structures in the shear layer at the cavity opening. These structures appeared to roll up then convect downstream. As they approached the aft wall they appeared to impact near the downstream corner of the cavity then be swept out and convected downstream past the cavity.
- Application of the POD for the resonating cavity showed that different POD modes corresponded to structures associated with different Rossiter modes.

8 References

Bassioni, I., Abdelkhalek, M., Ghoneim, Z., Daoud, M., Naguib, A., "Microphone-Array

Measurements of Acoustic and Hydrodynamic Wall Pressure Fluctuations in a Low-Speed Cavity Flow," AIAA Paper 2004-2655, 2004.

Bilanin, A. and Covert, E., "Estimation of Possible Excitation Frequencies for Shallow Rectangular Cavities," AIAA Journal, Volume 11(3), pp. 347-351, 1973.

Block, P. "Noise Response of Cavities of Varying Dimensions at Subsonic Speeds," NASA TN D-8351, 1976.

Cattafesta, L., Williams, D., Rowley, C. and Alvi, F., "Review of Active Control of Flow Induced Cavity Resonance," AIAA Paper 2003-3567, 2003.

Cole, D. and Glauser, M., "Applications of Stochastic Estimation in the Axisymmetric Sudden Expansion" Physics of Fluids, Vol. 10(11), pp. 2941-2949, 1998.

Disimile, P., Toy, N., and Savory, E., "Effect of Planform Aspect Ratio on Flow Oscillations in Rectangular Cavities," Journal of Fluids Engineering, Volume 100, pp. 32-38, 2000.

Gharib, M. and Roshko, A., "The Effect of Flow Oscillations on Cavity Drag," Journal of Fluid Mechanics, Volume 177, pp. 501-530, 1987.

Glauser, M.N., Taylor, J. A., Ukeiley, L. S., George, W. K. and Citriniti, J. H., "A Low Dimensional Description of the Axisymmetric Turbulent Jet: An Update," ERCOFTAC Bulletin, Vol. 46, pp. 53-61, 2000.

Grace, S. M., Dewar, W. G. and Wroblewshi, D. E., "Experimental Investigation of the Flow Characteristics within a Shallow Wall Cavity for Both Laminar and Turbulent Upstream Boundary Layers," Experiments in Fluids, Volume 36, pp.791-804, 2004.

Guezennec, Y., "Stochastic Estimation of Coherent Structures in Turbulent Boundary Layers," Physics of Fluids A, Vol. 1, No. 6, pp. 1054-60, 1989.

Hardin, J. and Mason, J., "Broadband Noise Generation by a Vortex Model of Cavity Flows," AIAA Journal, Volume 15(5), pp. 632-637, 1977.

Heller, H., Holmes, D. and Covert, E., "Flow-Induced Pressure Oscillations in Shallow Cavities," Journal of Sound and Vibration, Volume 18(4), pp. 545-553, 1971.

Heller, H. and Bliss, D., "The Physical Mechanisms of Flow Induced Pressure Fluctuations in Cavities and Concepts for Their Suppression," AIAA Paper 75-491, 1975.

Krishnamurty, K., "Acoustic Radiation from Two-Dimensional Rectangular Cutouts in Aerodynamic Surfaces," NACA TN-3487, 1955.

Lumley, J. L., "The Structure of Inhomogeneous Turbulent Flows," Atmospheric Turbulence and Radio Wave Propagation, (eds. Yaglom and Tatarsky), Nauka, Moscow, pp. 166-178, 1967.

Menon, S. and Kim, W.-W., \High Reynolds Number Flow Simulation Using the Localized Dynamic Subgrid Scale Model," AIAA Paper 96-0425, 1996.

Murray, R., and Elliot, G., "Characteristic of the Compressible Shear Layer Over a Cavity," AIAA Journal, Volume 39(5), pp. 846-856, 2001.

Murray, N., and Ukeiley, L., "Low-Dimensional Estimation of Cavity Flow Dynamics," AIAA Paper 2004-0681, 2004.

Murray, N., Time Resolved, Low-Dimensional Estimation of Open Cavity Flow," Masters Thesis, University of Mississippi, 2003.

Murray, N, E. and Ukeiley, L. S., "Estimation of the Flowfield From Surface Pressure

Measurements in an Open Cavity," AIAA Journal, Vol. 41, No. 5, pp 969-972, 2003.

Naguib, A., Wark, C. and Juckenhöfel, O., "Stochastic Estimation and Flow Sources Associated With Surface Pressure Events in a Turbulent Boundary Layer," *Physics of Fluids*, Vol. 13, No. 9, pp. 2611-26, 2001.

Picard, C., and Delville, J., "Pressure Velocity Coupling in a Subsonic Round Jet," Engineering Turbulence Modeling and Experiments – 4, edited by W. Rodi and D. Laurence, Elsevier, Amsterdam, pp. 443-452, 1999.

Rockwell, D. and Naudascher, E., "Review of Self-Sustained Oscillations of Flow Past Cavities," Journal of Fluids Engineering, Volume 100, pp. 152-165, 1978.

Roshko, A., "Some Measurements of the Flow in Rectangular Cut Outs," NACA TN 3488. 1955.

Rossiter, J., "Wind Tunnel Experiments on the Flow Over Rectangular Cavities at Subsonic and Transonic Speeds," Aeronautical Research Council, Reports and Memoranda No. 3438, 1964.

Rowley, C., Colonius, T. and Basu, A., "On Self-Sustained Oscillations in Two-Dimensional Compressible Flow Over Rectangular Cavities," Journal of Fluid Mechanics, Volume 455, pp. 315-346, 2002.

Schmidt, R., "Low Dimensional Tools for Flow-Structure Interaction Problems: Application to Micro Air Vehicles," Ph.D. Dissertation, Clarkson University, 2002.

Sinha, N., Hosangadi, A. and Dash, S., "The CRAFT NS Code and Preliminary Applications to Steady/Unsteady Reaction, Multi-Phase Jet/Plume Flowfield Problems," CPIA Pub. 568, May 1991.

Sinha, N., Arunajatesan, N. and Ukeiley, L., "High Fidelity Simulations of Weapons Bay Aeroacoustics and Active Flow Control," AIAA Paper 2000-1968, 2000.

Tam, C. and Block, P., "On the Tones and Pressure Oscillations Induced by Flow Over Rectangular Cavities," Journal of Fluid Mechanics, Volume 89(2), pp. 373-399, 1978.

Taylor, J., "Dynamics of Large Scale Structures in Turbulent Shear Layers," Dept. of Mechanical & Aeronautical Engineering, Clarkson University, NY, Rept. MAE-354, 2001.

Tracy, M., and Plentovich, E., "Cavity Unsteady-Pressure Measurements at Subsonic and Transonic Speeds," NASA Technical Paper 3669, 1997.

Ukeiley, L., Cole, D., and Glauser, M., "An Examination of the Axisymmetric Jet Using Coherent Structure Detection Techniques," In Eddy Structure Identification in Free Turbulent Shear Flows, Kluwer Academic Publishers (editors, J.P. Bonnet and M.N. Glauser) pp. 325-336, 1993.

Ukeiley, L., Seiner, J., Arunajatesan, S., Sinha. N. and Dash, S., "Low-Dimensional Description of Resonating Cavity Flow," AIAA Paper 2000-2459, 2000.

Ukeiley, L., Ponton, M., Seiner, J. and Jansen, B., "Suppression of Pressure Loads in Cavity Flows," AIAA Journal, Volume 42(1), pp. 70-79, 2004.